Draft version April 30, 2019
Typeset using LaTeX **twocolumn** style in AASTeX62

The Origin of [C II] 158 μm Emission toward the H II Region Complex S235

L. D. Anderson,[1,2,3] Z. Makai,[1] M. Luisi,[1,3] M. Andersen,[4] D. Russeil,[5] M. R. Samal,[6] N. Schneider,[7] P. Tremblin,[8] A. Zavagno,[5] M. S. Kirsanova,[9,10] V. Ossenkopf-Okada,[7] and A. M. Sobolev[10]

[1] *Department of Physics and Astronomy, West Virginia University, Morgantown WV 26506*
[2] *Adjunct Astronomer at the Green Bank Observatory, P.O. Box 2, Green Bank WV 24944*
[3] *Center for Gravitational Waves and Cosmology, West Virginia University, Chestnut Ridge Research Building, Morgantown, WV 26505*
[4] *Gemini South, Casilla 603, La Serena, Chile 0000-0002-5306-4089*
[5] *Aix Marseille University, CNRS, CNES, LAM, Marseille, France 13388*
[6] *Physical Research Laboratory, Navrangpura, Ahmedabad, Gujarat 380009, India*
[7] *I. Physikalisches Institut der Universität zu Köln, Zülpicher Straβe 77, 50937, Köln, Germany*
[8] *CEA-Saclay, Gif-sur-Yvette, France 91191*
[9] *Institute of Astronomy of the Russian Academy of Sciences, Moscow, Russia 119017*
[10] *Ural Federal University, Astronomical Observatory, Lenin 51, Ekaterinburg, Russia, 620083*

ABSTRACT

Although the $^2P_{3/2} - ^2P_{1/2}$ transition of [C II] at $\lambda \simeq 158\,\mu$m is known to be an excellent tracer of active star formation, we still do not have a complete understanding of where within star formation regions the emission originates. Here, we use *SOFIA* upGREAT observations of [C II] emission toward the H II region complex Sh2-235 (S235) to better understand in detail the origin of [C II] emission. We complement these data with a fully-sampled Green Bank Telescope radio recombination line map tracing the ionized hydrogen gas. About half of the total [C II] emission associated with S235 is spatially coincident with ionized hydrogen gas, although spectroscopic analysis shows little evidence that this emission is coming from the ionized hydrogen volume. Velocity-integrated [C II] intensity is strongly correlated with *WISE* 12 μm intensity across the entire complex, indicating that both trace ultra-violet radiation fields. The 22 μm and radio continuum intensities are only correlated with [C II] intensity in the ionized hydrogen portion of the S235 region and the correlations between the [C II] and molecular gas tracers are poor across the region. We find similar results for emission averaged over a sample of external galaxies, although the strength of the correlations is weaker. Therefore, although many tracers are correlated with the strength of [C II] emission, only *WISE* 12 μm emission is correlated on small-scales of the individual H II region S235 and also has a decent correlation at the scale of entire galaxies. Future studies of a larger sample of Galactic H II regions would help to determine whether these results are truly representative.

Keywords: H II regions – infrared: ISM – radio continuum: ISM – techniques: photometric

1. INTRODUCTION

The [C II] line is one of the most important transitions in the interstellar medium (ISM). This line arises from the $^2P_{3/2} - ^2P_{1/2}$ transition of ionized carbon at $\lambda \sim 158\,\mu$m (1.9 THz), at an equivalent temperature of $\Delta E/k_B \simeq 91.2$ K. Between 0.1 and 1% of the total FIR-luminosity of galaxies is provided by this emission line (Crawford et al. 1985; Malhotra et al. 1997; Boselli et al. 2002), a result that also holds for Galactic star formation regions (Stacey et al. 1991; Schneider et al. 1998). We observe [C II] emission from diffuse clouds, the warm ionized medium (WIM), the surface of molecular clouds, dense photodissociation regions (PDRs), and cold H I clouds (Pineda et al. 2013; Pabst et al. 2017). Since carbon has a lower ionization potential than hydrogen (11.3 eV vs. 13.6 eV), ionized carbon exists in a variety of environments, and can trace the $H^+/H/H_2$ transition layer.

[C II] emission is a good tracer of galactic star-formation rates (SFRs) in galaxies (De Looze et al.

Corresponding author: L.D. Anderson
loren.anderson@mail.wvu.edu

2011). They suggested, however, that [C II] emission cannot be used reliably as an SFR indicator for low-metallicity dwarf galaxies, and the scatter of the [C II]/SFR relationship increases as the galactic metallicity decreases. Since CO and [C II] emission are both correlated with the SFR, the connection between CO emission and [C II] intensities has been widely studied. Crawford et al. (1985) showed a strong linear relationship between the intensities of [C II] and ^{12}CO within gas-rich galaxies. Wolfire et al. (1989) found a tight linear correlation between the intensities of [C II] and CO in observations of both Galactic and extragalactic sources, suggesting a common origin of these lines.

Despite the strong [C II]/SFR relationship, there is still some doubt about where exactly the [C II] emission originates. A detailed study by Pabst et al. (2017) shows strong correlation between [C II] and *Spitzer* 8.0 μm emission from PDRs. Some additional information comes from the Galactic Observations of Terahertz C^+ ("GOT C^+" Langer et al. 2011) survey, a *Herschel* (Pilbratt et al. 2010) open time key project[1]. Using GOT C^+ data, Pineda et al. (2013) found that about half of [C II] emission (∼47%) is produced in regions of dense PDRs, 28% in dark H_2 gas, 21% in cold atomic gas, and just 4% in ionized hydrogen gas. The fraction of [C II] emission originating from the ionized phases of the ISM varies widely, from ∼ 5% to 50% depending on the electron density and ionizing radiation strength (Abel 2006). [C II] emission also arises in regions of diffuse neutral gas (Madden et al. 1993). GOT C^+ sparsely sampled the Galactic plane along 454 sight lines, in a variety of Galactic environments, but the lack of spatial information toward star formation regions makes their results difficult to generalize.

Since they make the ultraviolet (UV) photons that create C^+, the locations of massive stars should be strongly correlated with the locations of intense [C II] emission. The UV radiation from massive stars frequently creates ionized hydrogen, or "H II," regions. Dust within the regions absorbs and scatters high-energy photons. This leads to dust grain heating and subsequent emission of thermal photons in the mid- and far-infrared (MIR and FIR; e.g., Jones 2004; Relaño et al. 2016). Therefore, this process is sometimes referred to as "photon-destruction" (e.g., Krishna Swamy & O'dell 1967). The resulting lack of available H-ionizing photons has been shown to reduce the size of "dusty" H II regions (Sarazin 1977). Within an H II region, radiation pressure from the central source accelerates the dust grains outwards (Draine 2011; Akimkin et al. 2015, 2017).

Outside the ionized hydrogen zone of H II regions is a PDR, which is the boundary between the H II region and the interstellar medium. PDRs have a layered structure because interstellar dust shields species from far-UV (FUV) photons, and hence chemical stratifications are produced by the progressively weaker FUV-field (Ossenkopf et al. 2007). The "ionization front" is the boundary of the H II region, interior to which nearly all gas is ionized. Beyond the ionization front, hydrogen is predominantly neutral but carbon may be mostly ionized due to photons with energies between 13.6 eV and 11.3 eV. At the dissociation front, H_2 becomes the dominant species. Further from the ionizing source, where the material is more opaque to FUV-photons and the temperature is decreasing, ionized carbon recombines to produce atomic carbon and ^{12}CO, creating a transition layer of C^+/C/CO (cf. Hollenbach & Tielens 1999, their Figure 3).

Although the connection between [C II] and PDRs is well-established, the origin and distribution of [C II] emission toward individual H II regions in the Milky Way has received relatively little study. The few studies have have been done suggest that most of the [C II] emission toward H II regions arises from dense PDRs. In a study of the Orion B molecular cloud, Pabst et al. (2017) report that nearly all [C II] emission (∼95%) originates from the irradiated molecular cloud, with only a small (∼5%) contribution from the adjacent H II region (see also Pabst et al. 2019). Unlike Pineda et al. (2013), they do not make a clear distinction between PDRs and dark molecular gas. Their result is in rough agreement with Goicoechea et al. (2015) who found that 85% of the [C II] emission in the Orion molecular cloud 1 (OMC1) is produced on the surface of the molecular cloud. A smaller amount (∼ 15%) of the [C II] emission comes from a gas component not associated with CO. Goicoechea et al. (2018) also found support for [C II] emission arising from dense PDR gas in OMC1. Simon et al. (2012) observed the H II region complex S106 with the *Stratospheric Observatory for Infrared Astronomy* (*SOFIA*; Young et al. 2012) and found that part of the [C II] emission comes from the ionized hydrogen region since the locations of [C II] emission are similar to that of the cm continuum. A more recent study of S106 with *SOFIA*, however, argued that the [C II] emission is actually from the PDRs (Schneider et al. 2018). Graf et al. (2012) investigated the [C II] emission toward NGC2024 in the Orion B complex with *SOFIA* observations. They concluded that the observed ionized carbon comes from a highly clumpy interface between the molecular cloud and the H II region

[1] More information can be found on the GOT C^+ web site: https://irsa.ipac.caltech.edu/data/Herschel/GOT_Cplus/overview.html

and shows a good spatial correlation with the 8 μm continuum.

Here, we present *SOFIA* observations of the [C II] 158 μm line toward the massive star-forming complex Sh2-235, with the goal of understanding the origin of [C II] emission. S235 is a rich complex, with three separate H II regions and prominent PDRs. It therefore has the environments associated with strong [C II] emission. We can thus use the results from S235 to provide context to the results from external galaxies. We deal mainly with velocity-integrated [C II] emission; most of the detailed kinematics of the region will be discussed in a forthcoming paper.

2. THE SH2-235 STAR FORMATION COMPLEX

The Sh2-235 star forming complex (hereafter "S235;" Sharpless 1959) is located toward the Galactic anti-center. The distance to a water maser in the complex is $1.56^{+0.09}_{-0.08}$ kpc (Burns et al. 2015). This is roughly consistent with the recent GAIA DR2 parallax of the ionizing source of S235 BD+351201 (Brown 2018), which corresponds to a distance of 1.73 ± 0.13 kpc. Here, we adopt a distance of 1.6 kpc for the region. Since its first appearance in scientific literature (Minkowski 1946), it has been extensively studied from the optical through radio regimes (e.g., Evans & Blair 1981; Nordh et al. 1984; Allen et al. 2005; Kirsanova et al. 2008; Boley et al. 2009; Camargo et al. 2011; Kirsanova et al. 2014; Bieging et al. 2016; Dewangan & Ojha 2017).

In this paper, we study three main regions of the S235 complex (Figure 1). The main S235 region H II region (Sh2-235) which we call "S235MAIN" is ionized by an O9.5V star BD+351201 (Georgelin et al. 1973). Active star formation is continuing in S235MAIN, as it hosts more than 200 young stellar objects (YSOs; Dewangan & Anandarao 2011). S235MAIN hosts the IR sources IRS1 and IRS2 (Evans & Blair 1981), both of which are created by B-type stars.

There are two smaller H II regions to the south of S235MAIN: S235A and S235C (Israel & Felli 1978). S235A is located $\sim 10'$ (~ 4 pc) south of S235MAIN, and is also known as IRS3 (Evans & Blair 1981) and radio source G173.72+2.70 (Israel & Felli 1978). S235A has methanol and water masers (see Chavarría et al. 2014, and references therein), and is known as an expanding H II region ionized by stars of main sequence spectral types between B0 and O9.5 (e.g., Felli et al. 1997). Near to S235A is the reflection nebula S235B (IRS4) caused by a B-type star (Boley et al. 2009). We refer to S235A and S235B combined as the star forming region "S235AB" since they are not separated at the angular resolution of our data. S235C is located $\sim 5'$ (~ 2 pc) south of S235A and is ionized by a B0.5 star (see Table 1 in Bieging et al. 2016). Dewangan & Ojha (2017) showed that these smaller star formation regions are interacting with the surrounding molecular clouds, and that star formation may be triggered by the expansion of the H II region (e.g., Kirsanova et al. 2008; Camargo et al. 2011). Kirsanova et al. (2014) suggested that the star formation in S235AB is not related to the expansion of S235MAIN.

The S235 complex is an ideal target for studies of [C II] emission. It is nearby, bright, and has been the focus of many previous studies. It also contains three separate H II regions, two of which are compact. The size of H II regions depends on their age and the intensity of ionizing radiation. Therefore, we can examine differences in [C II] emission for H II regions of different ages and ionizing radiation fields.

3. DATA

3.1. *SOFIA* [C II] *and* [N II] *data*

We observed [C II] and [N II] emission toward the S235 complex in *SOFIA* Cycles 4 and 5 in November 2016 and February 2017 using the *SOFIA* upGREAT instrument (Risacher et al. 2016). upGREAT is an enhanced version of the German Receiver for Astronomy at Terahertz Frequencies (GREAT; Heyminck et al. 2012). We used the upGREAT LFA channel (a 7 pixel array in 2016 and a 2×7 pixel array in 2017) to tune to [C II] and the L1 (single pixel) channel to tune to the $^3P_1 - ^3P_0$ [N II] 205 μm (1.46 THz) line. The total observing time for both cycles was 3.5 hours. We observed in total power on-the-fly (OTF) mapping mode and mapped a total area of $0.^\circ21 \times 0.^\circ37$ ($\alpha \times \delta$), centered at ($\alpha, \delta[J2000]$) = (5h41m02.5s, 35°51m57s). We employed a fast mapping mode for S235MAIN, which resulted in an undersampled map for [N II], and a slow mapping mode for S235AB and S235C, which resulted in a fully-sampled [N II] map. The spatial resolution of the [C II] data is 14.8″, the velocity resolution is 0.385 km s^{-1}, and the full velocity range is −60 to 20 km s^{-1}. The spatial resolution of the [N II] data is 20.2″, the velocity resolution is 0.500 km s^{-1}, and the full velocity range is −60 to 20 km s^{-1}.

The final data cubes provided by the SOFIA Science Center (in units of main beam temperature T_{MB}) were processed using the Grenoble Image and Line Data Analysis Software (GILDAS)[2]. The data were first scaled to T_A^*, the antenna temperature corrected for atmospheric opacity, using a forward efficiency of 0.97.

[2] http://iram.fr/IRAMFR/GILDAS/ (Pety 2005)

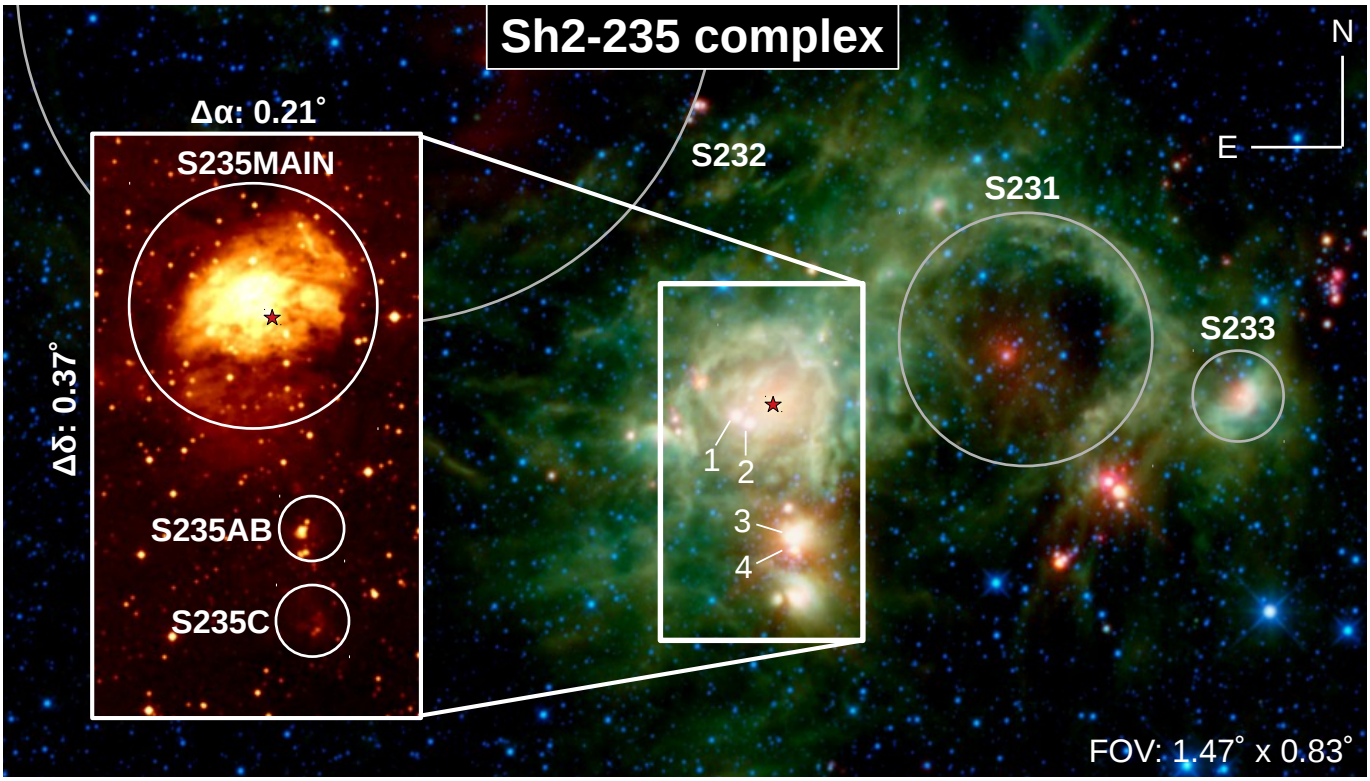

Figure 1. S235 star forming complex in a four-color *WISE* image created by NASA/JPL-Caltech/*WISE* Team. Red, green, blue and cyan correspond to infrared wavelengths of 22 μm, 12 μm, 4.6 μm, and 3.4 μm, respectively. The total field of view (FOV) is $1\overset{\circ}{.}47 \times 0\overset{\circ}{.}83$, oriented in RA and Decl., and centered near $(\alpha, \delta(\mathrm{J2000}))$ = (05:41:16, +35:50:52). All Sharpless H II regions in the field are identified. Numbers 1–4 indicate infrared IRS sources from Evans & Blair (1981) and the red star indicates the location of the ionizing source of S235. The inset shows DSS red data showing emission from ionized gas in the area we investigate in this paper, which has a FOV of $0\overset{\circ}{.}21 \times 0\overset{\circ}{.}37$. Circles denote the main S235 H II region (S235MAIN, upper circle) that contains the inner ionized hydrogen region and the surrounding PDRs, and the two smaller H II regions (S235AB and S235C, two lower circles). S235AB contains the S235A H II region and the S235B reflection nebula; these we treat as one star formation region.

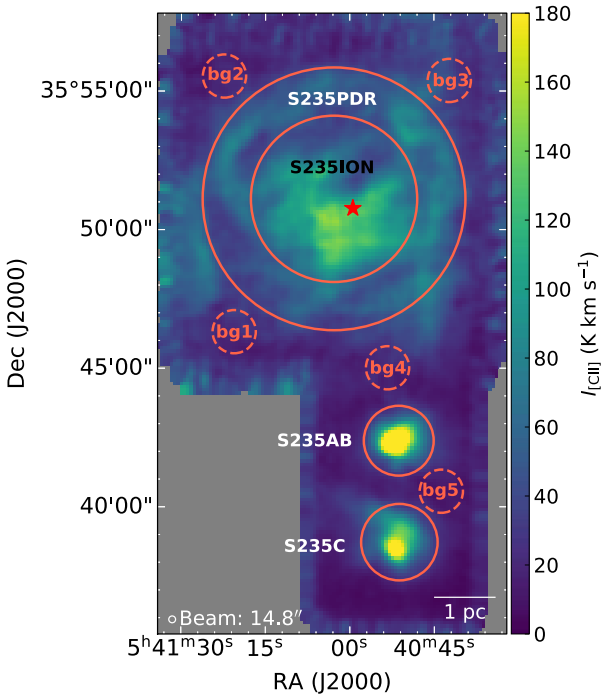

Figure 2. Integrated (-29 to -12 km s^{-1}) intensity map of *SOFIA* [C II] 158 μm data, smoothed by a 3×3 pixel Gaussian kernel (approximately the beam size). The red circles enclose regions of interest, with dashed circles denoting background regions. The filled red star marks the position of the ionizing source BD+351201. The smaller H II regions show strong and compact [C II] emission.

Antenna temperature values were converted to main beam temperatures using the main beam efficiency of $\eta_{\rm MB} = 0.69$. If the rms of an individual spectrum was higher than two times the radiometer noise, the spectrum was ignored. First order (if rms < radiometer noise) or third order (if rms < 2 × radiometer noise) baselines were removed from all spectra.

Here, we frequently use the integrated [C II] intensity, "moment 0," from the velocity range -29 to -12 km s^{-1} (Figure 2). All significant [C II] emission associated with S235 is found within this velocity range (see Figure 5). This figure shows strong [C II] emission from the PDRs surrounding S235, but the most intense emission in the field is found toward S235AB and S235C.

[N II] is only weakly detected when averaged over the entire ionized hydrogen region. Because there is little spatial information on the distribution of [N II], we limit analyses using these data.

3.1.1. *Regions of interest*

Using the [C II] moment 0 map as a guide, we determine regions of interest in the S235 field. For S235MAIN, we define one region of interest spatially coincident with the ionized hydrogen gas ("S235ION"), and an annular region surrounding the ionized hydrogen gas that contains most of the plane-of-sky PDR emission ("S235PDR"). We define regions of interest for the two smaller H II regions located to the south of S235MAIN ("S235AB" and "S235C"). We also sample diffuse emission in the field using five smaller background regions ("bg1–5"). We list the parameters of these regions of interest in Table 1.

Table 1. Parameters of the regions of interest

Region	α_{J2000}	δ_{J2000}	Radius
	h:m:s	d:m:s	″
S235PDR	5:41:02.76	35:51:06.48	284.4[a]
S235ION	5:41:02.76	35:51:06.48	187.2
S235AB	5:40:51.24	35:42:23.04	75.6
S235C	5:40:51.24	35:38:42.36	82.8
bg1	5:41:20.40	35:46:19.20	46.8
bg2	5:41:22.20	35:55:32.52	46.8
bg3	5:40:42.24	35:55:22.80	46.8
bg4	5:40:53.40	35:45:00.72	46.8
bg5	5:40:43.68	35:40:33.60	46.8

[a]The S235PDR region is annular, with its inner radius equal to the radius of S235ION. The value listed here represents the outer radius.

3.2. *Green Bank Telescope Radio Recombination Line Maps*

To understand the distribution and velocity structure of the ionized gas, we create a fully-sampled map in 6 GHz radio recombination line (RRL) emission using the Green Bank Telescope (GBT). The region has been observed previously in H-α by Lafon et al. (1983), who found a strong velocity gradient in the ionized hydrogen gas; the velocity is ~ -15 km s^{-1} in the south-east of the region (near our "bg1" region) and ~ -25 km s^{-1} in the north-west (near our "bg3" region). This strong gradient is unusual for an H II region and may be due in part to absorption of H-α emission or to a bulk "champagne flow" of ionized gas.

We follow the same observing setup as in Anderson et al. (2018) and Luisi et al. (2018), tuning to 64 different frequencies at two polarizations within the 4−8 GHz receiver bandpass. Of these 64 tunings, 22 are H$n\alpha$ transitions from $n = 95$ to $n = 117$. Carbon and helium RRLs fall within the same bandpass as that of hydrogen, shifted by -149.56 km s^{-1} and -122.15 km s^{-1} from hydrogen, respectively. Carbon RRLs are thought

to arise from PDRs surrounding H II regions, whereas helium RRLs come from the ionized hydrogen region.

There are 15 usable Hnα lines after removing those spoiled by radio frequency interference (RFI) or instrumental effects. Over the frequencies of the usable Hnα lines, the beam size ranges from 98″ to 183″, with an average of 141″. We calibrate the intensity scale of our spectra using noise diodes fired during data acquisition and assume a main beam efficiency of 0.94.

The map is $0.8^\circ \times 0.7^\circ$, centered at $(\alpha, \delta[J2000]) =$ (5h40m42s, +35°48m52s). We create four complete maps, two in RA and two in Dec., to mitigate in-scan artifacts, and average all together.

We average all lines at a given position to make one sensitive spectrum (Balser 2006), a technique that is well-understood (Anderson et al. 2011; Liu et al. 2013; Alves et al. 2015; Luisi et al. 2018). After removing transient RFI, we remove a polynomial baseline for each transition and shift the spectra so that they are aligned in velocity (Balser 2006). We re-grid the 15 good Hnα lines to a velocity resolution of 0.5 km s^{-1} and a spatial resolution of 1′. We then average the individual maps using a weighting factor of $t_{\rm intg} T_{\rm sys}^{-2}$ where $t_{\rm intg}$ is the integration time and $T_{\rm sys}$ is the system temperature.

We show the integrated intensity moment zero hydrogen RRL map in Figure 3. The emission is strongest for S235MAIN and peaked at the location of the ionizing source. S235AB also shows detected emission, but S235C does not. The other H II regions in the field have some detected RRL emission. We show the peak line velocity derived from Gaussian fits in Figure 5, although due to the relatively poor spatial resolution we do not show the fit for S235PDR. For S235ION, the fit is to the average spectrum from our RRL map integrated over the entire region of interest. For S235AB and S235C, we use the pointed RRL results from Anderson et al. (2015), because the signal to noise in the RRL map is rather poor and the observational setup in Anderson et al. (2015) is the same as ours used here.

3.3. *Ancillary data*

We also use *WISE* MIR, 1.4 GHz NVSS radio continuum, and CO rotational transitions to investigate the S235 region (Figure 4). For later comparisons, we regrid all ancillary data to 10″ pixels, and do the same for the *SOFIA* [C II] data. The CO data in panels (d), (e), and (f) of this figure are of integrated intensity, integrated over −29 to −12 km s^{-1} as we did for [C II] (Figure 2).

3.3.1. *WISE 12 μm and 22 μm data*

WISE (Wright et al. 2010) mapped the entire sky at four wavelengths: 3.4 μm, 4.6 μm, 12 μm and 22 μm. The angular resolutions are 6.″1, 6.″4, 6.″5 and 12″ with

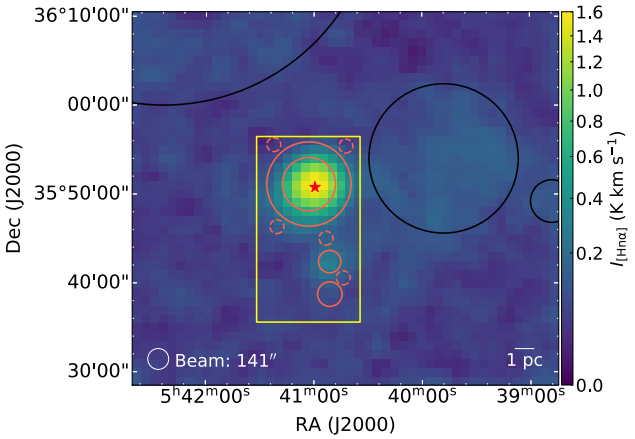

Figure 3. Integrated (−29 to − 12 km s^{-1}) intensity map of GBT RRL data. The yellow rectangle shows the extent of the *SOFIA* [C II] data (Figure 2). As in Figure 2, the red circles enclose regions of interest, with dashed circles denoting background regions. Black circles enclose other H II regions in the field (cf. Figure 1). The filled red star marks the position of the ionizing source BD+351201. The strongest RRL emission comes from S235MAIN, although S235AB is also bright and there is detectable emission from the other regions in the field.

5σ point-source sensitivities of 0.08 mJy, 0.11 mJy, 1 mJy and 6 mJy at the native pixel scales, respectively. We use here the 12 μm and 22 μm bands. The 12 μm band is sensitive to the emission from polycyclic aromatic hydrocarbon (PAH) features at 11.2 μm, 12.7 μm, and 16.4 μm (e.g., Roser & Ricca 2015; Tielens 2008). Due to high expected optical depth in this wavelength range, the *WISE* 12 μm band is likely a *surface*, rather than volume tracer, in contrast to the some of the other ancillary data used here. The W4 22 μm bandpass is sensitive to stochastically-heated very small grains (VSGs) within the H II region plasma, and also to dust grains within the PDRs (PAHs are prominent contributors of 24 μm emission; see Robitaille et al. 2012).

The *WISE* data have "Digital Number" (DN) units and we used the DN-to-mJy conversion factors of 2.9045×10^{-3} and 5.2269×10^{-2} for the 12 μm and 22 μm data, respectively[3]. We use the color-correction of Wright et al. (2010), assuming a spectral index of $\alpha = 0$. This correction increases the 12 and 22 μm flux densities by 9.1% and 1.0%, respectively.

The 12 μm data show the same spatial distribution as [C II] throughout the field, including for the smaller H II regions to the south (see panel (a) in Figure 4). In the PDR of S235, the 12 μm emission follows the filamentary

[3] For more information, see http://wise2.ipac.caltech.edu/docs/release/prelim/expsup/sec2_3f.html

distribution of the ionized carbon. The *WISE* 22 μm emission (panel (b) in Figure 4) is centrally concentrated for S235, with comparatively faint emission in the PDRs. The 22 μm emission for S235AB and S235C is compact.

3.3.2. *NVSS 1.4* GHz *continuum data*

The ionized gas of H II regions emits in radio continuum due to free-free (Bremsstrahlung) radiation. We obtained 1.4 GHz radio continuum data from the NRAO VLA Sky Survey[4] (NVSS; Condon et al. 1998). The NVSS FWHM synthesized beam size is $\sim 45''$ and its rms uncertainty is ≈ 0.45 mJy/beam. During the regridding process, we convert the NVSS data from their native units of Jy beam^{-1} to mJy pixel^{-1}, the same as we use for our *WISE* data.

Similar to the RRL and 22 μm band data, the radio continuum emission (panel (c) in Figure 4) is concentrated around the ionizing source. That the [C II] and radio continuum distributions differ shows that we observe two different ionized phases of the ISM along the line of sight.

3.3.3. *CO data*

The ancillary molecular line data used here of ^{12}CO $2-1$, ^{12}CO $3-2$, and ^{13}CO $2-1$ are from Bieging et al. (2016). The observations were made with the Heinrich Hertz Submillimeter Telescope[5] in March to April, 2010. The two $J = 2-1$ lines were observed simultaneously. The ^{12}CO emission line was observed in the upper sideband, while the ^{13}CO line at 220.399 GHz was observed in the lower sideband. The maps cover $\sim 1.^{\circ}2 \times 0.^{\circ}8$ (α, δ), have a velocity resolution of 0.3 km s^{-1}, and have a spatial resolution of $38''$.

The ^{12}CO $3-2$ line was observed in April, 2014, also with the Heinrich Hertz Submillimeter Telescope, using the multi-pixel focal plane array of superconducting mixers ("SuperCam"; Kloosterman et al. 2012). The FWHM beam width is $24''$. The total area covered is $\sim 0.^{\circ}3 \times 1.^{\circ}0$ (α, δ) with 0.23 km s^{-1} velocity resolution.

Kirsanova et al. (2008) distinguished three main velocity components in the S235MAIN region using ^{13}CO $1-0$ and CS $2-1$ observations: a "red" component ($-18 < V_{lsr} < -15$ km s^{-1}), a "central" component ($-21 < V_{lsr} < -18$ km s^{-1}) and a "blue" component ($-25 < V_{lsr} < -21$ km s^{-1}). With additional observations of NH_3, Kirsanova et al. (2014) confirmed the existence of these different velocity components. Using ^{12}CO $1-0$ data, Dewangan & Ojha (2017) reported that the emission toward S235MAIN peaks in the velocity range -22 to -20, while the smaller H II regions, S235A ("S235AB") and S235C, are at ~ -17 km s^{-1}.

The ^{12}CO $2-1$ data have a broad velocity component (centered at ~ -11.5 km s^{-1}) that is well-separated from the aforementioned velocity components, but is absent in the other molecular and [C II] line data (see Figure 5). This redshifted component is possibly related to more diffuse gas not associated with S235; the component is also prominent in EBHIS H I emission (Winkel et al. 2016). As this component is redshifted relative to the overall velocity of the star-forming region S235, we likely observe the diffuse molecular gas component foreground or background to the star formation complex.

The CO moment maps have similar spatial distributions (see panels (d), (e) and (f) in Figure 4). The molecular emission is more extended than that of [C II], but components associated with the ionized hydrogen zone and the PDR of S235MAIN are clearly visible. The spatial distributions of the observed molecular gas tracers shows a bridge between S235AB and S235C, especially in case of the denser gas tracer ^{13}CO $2-1$. As these small H II regions are essentially at the same velocity, this indicates that S235AB and S235C might be physically connected by a dense gas component.

In the S235PDR region the spatial correlation of the observed [C II] and molecular gas is weaker than in the inner ionized hydrogen region. The CO emission appears clumpy compared to the emission of the other tracers. CO emission is absent toward the north. This "emission-free" part can also be seen in previous studies (e.g., Dewangan et al. 2016; Dewangan & Ojha 2017). This molecular deficit may be due to escaping ionized hydrogen gas in this direction (Dewangan et al. 2016). Although there is no indication that ionized hydrogen gas fills the evacuated space (see radio continuum map, panel (c) of Figure 4), the gas may be too rarefied to produce strong radio continuum emission.

3.4. *Velocity structure of* [C II] *emission*

We compare the spectra of [C II] (Section 3.1), RRL (Section 3.2), and CO (Section 3.3.3) emission from the regions of interest in Figure 5. The [C II] emission peaks near -20 km s^{-1} for S235MAIN, and -18 km s^{-1} for S235AB and S235C. All significant [C II] emission is in the range -29 to -12 km s^{-1}. Hydrogen RRL emission is much broader than that of the other tracers. It peaks near -23 km s^{-1} for S235ION an near -16 km s^{-1} for S235AB and S235C. Quireza et al. (2006) found that H RRLs toward S235ION peak at -23.07 km s^{-1} and C RRLs peak at -19.82 km s^{-1} (Silverglate & Terzian 1978; Vallee 1987, see also). An-

[4] https://www.cv.nrao.edu/nvss/

[5] For more information, see: http://aro.as.arizona.edu/smt_docs/smt_telescope_specs.htm

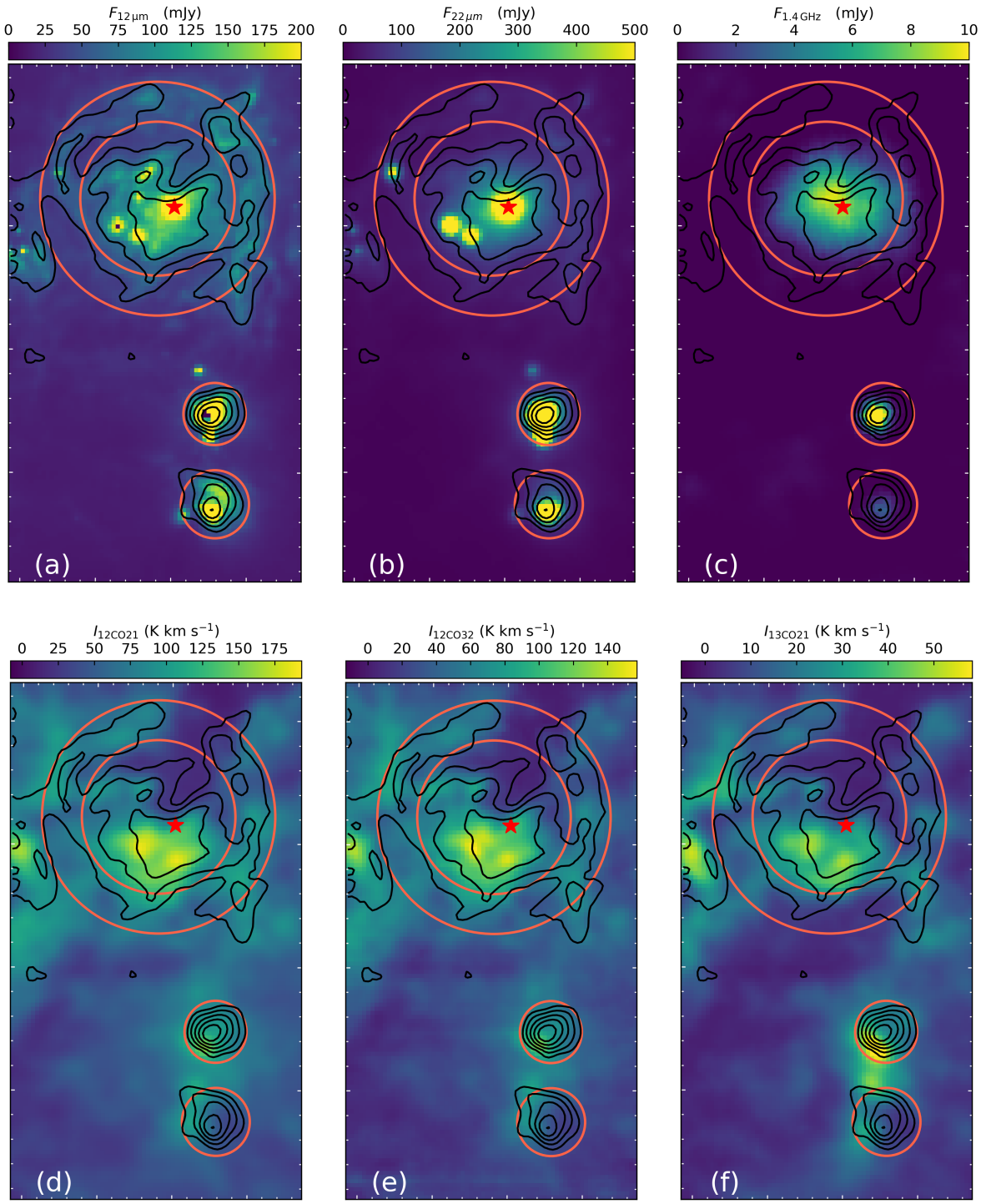

Figure 4. Flux density maps of *WISE* 12 μm and 22 μm ((a) and (b), respectively), flux density map of 1.4 GHz radio continuum (c), and integrated (-29 – -0.7 km s^{-1}) intensity maps of ^{12}CO 2 – 1 (d), ^{12}CO 3 – 2 (e), ^{13}CO 2 – 1 (f). The covered area is the same as on Figure 2. Black contours are of [C II] data at values of 15%, 25%, 40%, 60%, and 85% of the peak [C II] integrated intensity. As in Figure 2, red circles denote regions of interest (see Section 3.1.1) and the red filled star denotes the central ionizing source of S235MAIN. Much of the CO emission arises from the close vicinity of the central ionizing source. The 12 μm emission has a good spatial correlation with [C II], whereas the CO emission is more widespread than that of [C II], and the 22 μm and 1.4 GHz emission are more compact.

derson et al. (2015) found that the RRL emission from S235A peaks at -15.3 km s^{-1}, and that of S235C peaks at -16.6 km s^{-1}. The CO emission has a similar velocity profile to that of [C II], and carbon RRLs also peak near the velocities of strongest CO emission. We conclude that there is a real offset between the H RRL emission and that of other tracers in S235ION. This offset is not seen in the other regions of interest.

The [C II] emission can be decomposed into three velocity ranges: -23 to -20 km s^{-1} ("low"), -20 to -18 km s^{-1} ("middle"), and -18 to -13 km s^{-1} ("high"). These three ranges have distinct emission components. We show moment maps of these three velocity ranges in Figure 6. The low velocity range contains bright compact [C II] emission in the ionized hydrogen region of S235MAIN, emission from the eastern PDR, and a ridge of emission extending to the northwest. The middle velocity range contains multiple knots of compact [C II] emission in the ionized hydrogen region of S235MAIN, and emission from the PDR to the northeast and to the west. The high velocity range mainly contains [C II] emission from the western PDR of S235MAIN, and also compact emission from S235AB and S235C. Although S235AB and S235C are detected in the middle velocity range, this is just the blueshifted wing of emission (see Figure 5). All velocity components show excellent spatial agreement with ^{12}CO $2-1$ emission.

4. CORRELATIONS BETWEEN [C II] AND ANCILLARY DATA

Below, we determine correlations between [C II] intensity and the intensity of the ancillary data sets. We are dealing with emission integrated along the line of sight, and so in the direction of the ionized hydrogen gas we also detect emission from the front- and backside PDRs. This is especially important for the 12 μm emission, as it is a strong PDR tracer. For example, the region S235ION contains dense molecular clumps S235 Central E and Central W (Kirsanova et al. 2014; Dewangan & Ojha 2017). These clumps are presumably do not reside within the ionized hydrogen volume, but nevertheless the emission associated with the clumps is contained in the S235ION region of interest.

The NVSS and RRL data both trace the emission from ionized gas in the region. The spatial resolution of the NVSS is more than twice as fine as that of our RRL data. We therefore use the NVSS for all spatial analyses, and use the RRL data for all spectral analyses.

4.1. *Total fluxes in regions of interest*

We give the total fluxes for the regions of interest in Table 2. We find these values by integrating the emission

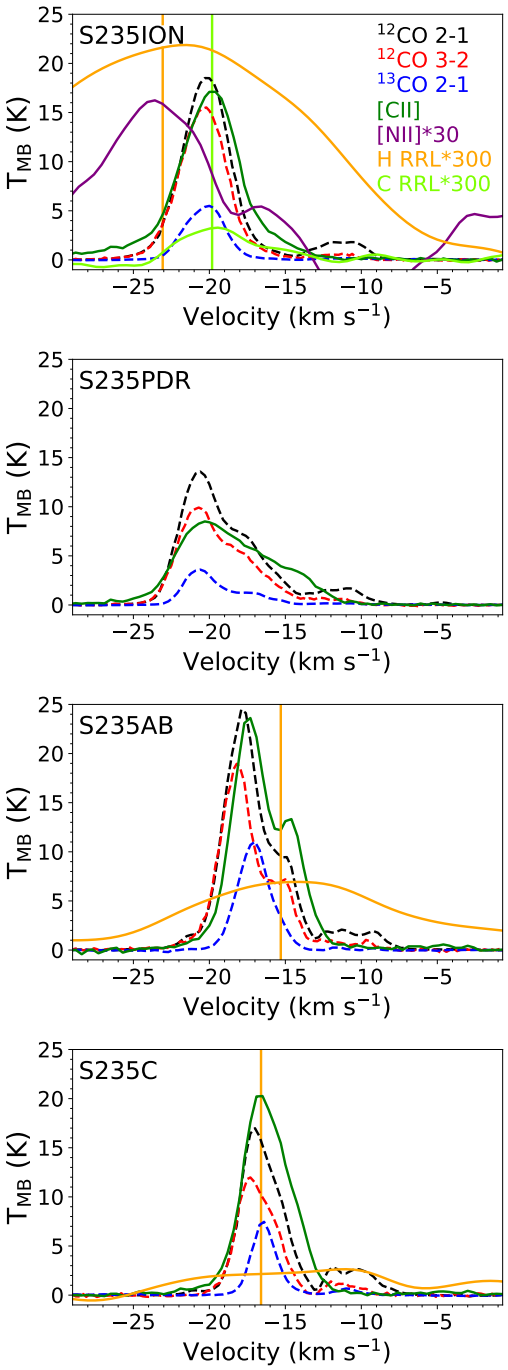

Figure 5. Spatially averaged spectra from the regions of interest for molecular gas tracers from Bieging et al. (2016) (^{12}CO ($J=2-1$), ^{12}CO ($J=3-2$), and ^{13}CO ($J=2-1$) in black, red and blue dashed lines, respectively), *SOFIA* [C II] and [N II] emission (green and purple curves, respectively), and GBT hydrogen and carbon RRLs (orange and light green curves, respectively). We smoothed the [N II] data with a 2.5 km s^{-1} FWHM Gaussian. The H and C RRL data have been smoothed with Gaussians of FWHM 5 km s^{-1} and 2.5 km s^{-1}, respectively. Vertical orange and green lines show the peak hydrogen and carbon RRL velocities as found in the literature. [N II] is only detected toward S235ION and the emission from S235PDR is not resolved in the RRL data so no RRL emission is shown in that panel.

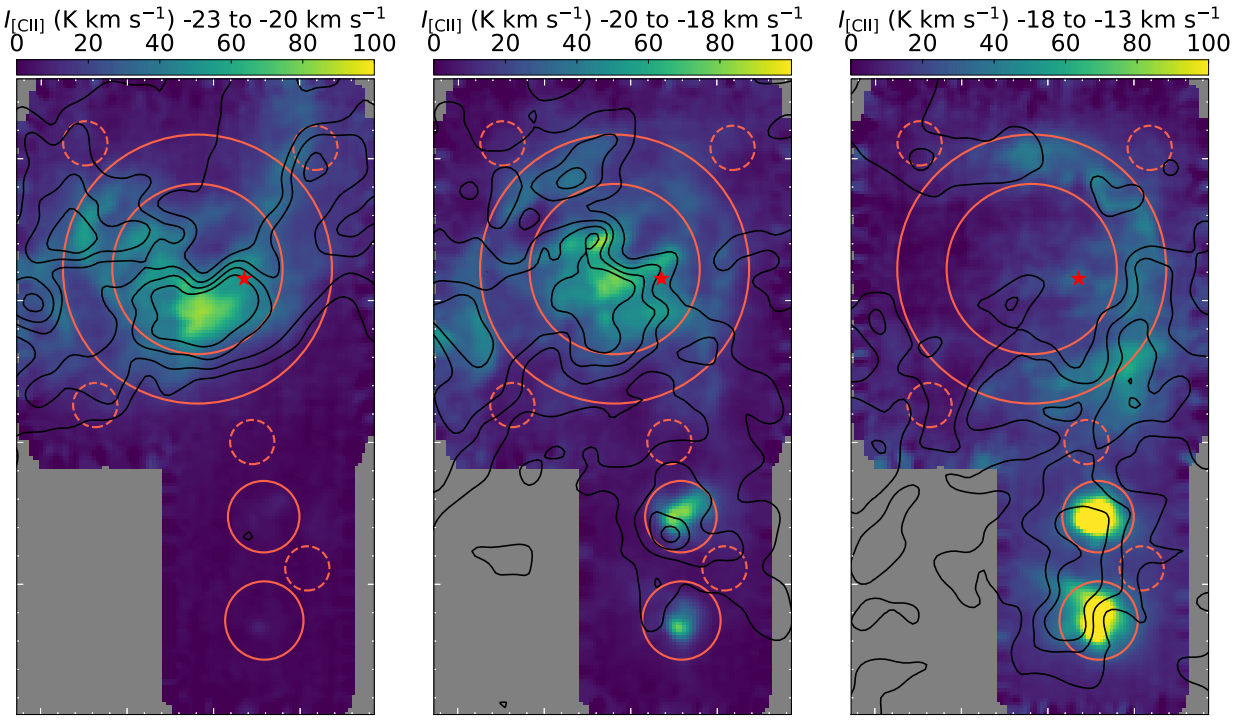

Figure 6. Moment maps of [C II] emission over three velocity ranges: -23 to -20 km s^{-1} (left), -20 to -18 km s^{-1} (middle), and -18 to -13 km s^{-1} (right). These three velocity ranges have distinct emission components. The field of view in each panel is the same as that of Figure 2. Contours show ^{12}CO 2 − 1 emission integrated over the same velocity ranges. There is excellent spatial agreement between the [C II] and CO emission.

Table 2. Fluxes from regions of interest

Region	$F_{[C\,II]}$	$F_{12\,\mu m}$	$F_{22\,\mu m}$	$F_{1.4\ GHz}$	F_{12CO21}	F_{12CO32}	F_{13CO21}	Area
	10^{-12} W m^{-2}	Jy	Jy	Jy	10^{-15} W m^{-2}	10^{-15} W m^{-2}	10^{-15} W m^{-2}	sq. arcmin.
S235MAIN	2.9	310	1000	1.9	5.7	14	1.0	71
S235ION	1.5	160	520	1.9	2.7	6.9	0.54	31
S235PDR	1.4	150	520	0.022	3.0	6.8	0.46	40
S235AB	0.30	40	150	0.33	0.62	1.5	0.17	5.0
S235C	0.27	33	110	0.051	0.41	0.86	0.088	6.0

over each aperture as defined in Table 1. For [C II] and the molecular tracers, the data are in units of main beam temperature, T_{MB}, so the integrated intensity $I_{[C\,II]} = \int T_{MB} dv$ has units of K km s^{-1}. We convert the [C II] and CO data to the more useful quantity of flux in units of W m^{-2} per pixel. For our *SOFIA* [C II] maps with 7″ pixels, the conversion between integrated intensity and flux for each pixel is

$$\frac{F_{[C\,II]}}{\mathrm{W m^{-2}}} = 8.1 \times 10^{-18} \frac{I_{[C\,II]}}{\mathrm{K\ km\,s^{-1}}}\,. \quad (1)$$

We subtract a local background value from the two *WISE* bands, computed as the median value surrounding the region, but perform no background correction for the other data.

The $I_{[C\,II]}$ and $F_{12\,\mu m}$ values appear in roughly the same ratio for all regions of interest. This correlation is less strong for the other tracers. We will explore this in more detail in Section 4.3.

We see from Table 2 that about half the emission from S235MAIN comes from the S235PDR region of interest for [C II], the MIR bands, and all CO transitions. The [C II] emission is strong south of the ionizing source (see Figure 2). The [C II] emission in a central zone 1.5′ in radius around the ionizing source has an integrated intensity of $\sim 0.6 \times 10^{-12}$ W m^{-2}, which is $\sim 40\%$ that

of S235ION and $\sim$ 20% that of the total emission from S235MAIN.

The values for all tracers are similar for S235AB and S235C, except for the radio continuum data. S235AB has $\sim$ 6 times higher flux density than S235C, indicating a higher Lyman continuum photon production rate in S235AB, a higher optical depth in S235C, and/or stronger dust absorption in S235C.

For S235MAIN, roughly half of the integrated intensity in all CO transitions is coming from the S235ION region, and half from the S235PDR region. In all the observed molecular transitions, the S235AB region is marginally brighter than S235C.

4.2. [C II] *emission from front- and back-side PDRs*

Because of emission from front- and back-side PDRs along the line of sight, it is difficult to accurately determine the percentage of [C II] emission from the entire PDR of S235. Based on results from previous studies of H II regions in [C II] emission, we expect that nearly all the [C II] emission arises from dense PDRs (e.g., Pabst et al. 2017).

In Figure 7 we show position-velocity (p-v) diagrams for S235MAIN. These diagrams show [C II] emission from the S235ION region in red and from S235PDR in cyan. We create the orange (from H RRL data) and green (from C RRL data) crosses in this figure by integrating the RRL data along its position axes, and then fitting Gaussians spaxel by spaxel.

Based on its coincidence with CO and the velocity offset of the ionized hydrogen gas with respect to all other tracers, we believe that the [C II] emission seen toward the ionized hydrogen is from line-of-sight PDRs and not from the ionized hydrogen volume. The peak velocity of [C II], CO, and C RRL emission toward the ionized hydrogen gas is redshifted relative to that of the ionized hydrogen gas itself, whereas [C II] and CO emission from the PDR is at a similar velocity to that of the ionized hydrogen gas. In support of this, we note the excellent spatial agreement between [C II] and CO emission in the three velocity ranges shown in Figure 6. This is consistent with an expansion of the ionized hydrogen gas preferentially toward us. In this scenario, the [C II], CO, and C RRL emission are therefore due to back-side PDRs, as we draw in the cartoon model of Figure 8. This explanation is consistent with the fact that minimal absorption is seen across the face of the region in H$-\alpha$ maps (see Figure 1; also Dewangan & Ojha 2017, their Figure 10b). If there were dense foreground PDR material, we would see H-α absorption across the face of the region, which we do for H II regions RCW120 (see Anderson et al. 2015, their Figure 1) and M20 (the Trifid Nebula; see Rho et al. 2006, their Figure 1). Our picture of S235 is similar to the model of Orion in Pabst et al. (2019, cf. their Figure 3). The main difference is that they observe a shell of [C II] expanding toward us, whereas in S235 we see no evidence for such a feature.

We can also use the measured [C II] and [N II] intensities to estimate the fraction of [C II] emission that arises from neutral hydrogen regions. Croxall et al. (2017) found that the [C II] to [N II] intensity ratio has a value of $I_{[\mathrm{C\,II}]}/I_{[\mathrm{N\,II}]} \simeq 4$ for ionized gas, independent of electron density. Values of $I_{[\mathrm{C\,II}]}/I_{[\mathrm{N\,II}]} > 4$ indicate [C II] emission from regions of neutral hydrogen. From the S235ION region, we measure $I_{[\mathrm{N\,II}]} \simeq 2 \times 10^{-13}\,\mathrm{W\,m^{-2}}$, which gives us $I_{[\mathrm{C\,II}]}/I_{[\mathrm{N\,II}]} \simeq 10$ (see Table 2). Using Equation 1 from Croxall et al. (2017), this results in a fraction of [C II] emission from neutral hydrogen regions $f_{[\mathrm{C\,II}],\mathrm{Neutral}} \simeq 0.5$. Because of the low quality of our [N II] data, this value is only approximate. Our intensity ratio, however, is roughly consistent with that observed in the external galaxy sample of Croxall et al. (2017) and the study of Rigopoulou et al. (2013). If half of the [C II] emission towards S235ION comes from locations of neutral hydrogen, just 25% of the emission from all of S235MAIN is from the ionized hydrogen volume.

4.3. *Correlations with* [C II] *intensities*

We investigate the correlation between [C II] intensity and that of the other tracers to help determine the origin of the [C II] emission. We plot pixel-by-pixel correlations of the regridded data (Figures 9, 10, A.1, and A.2) to examine the relationships between the integrated intensity of [C II] and that of the other tracers in the S235MAIN (S235ION and S235PDR), S235AB, and S235C regions. The bottom panel of each figure contains all data points, one per pixel of the regridded maps.

To quantify the relationships between [C II] and other observed tracers, we fit linear regressions of the form $I_{[\mathrm{C\,II}]} = A + B \times I_\lambda$, where $I_{[\mathrm{C\,II}]}$ is the integrated intensity of [C II], I_λ is the integrated intensity of CO or the flux density for the IR and radio continuum data. We use a robust least-squares method to determine the fit parameters, with a Cauchy loss function. The robust least squares fit minimizes the influence of outliers, which otherwise can skew the results. For data with few outliers, the choice of loss function has minimal impact on the fit parameters. We have left the data in their natural units, so B has units of K km s^{-1}/mJy for the *WISE* and NVSS data, and is unitless for the CO data. We compute the coefficient of determination R^2 and list these values and the fit parameters in Table 3.

Based on previous results, we expect that this linear relationship can approximate the correlation between

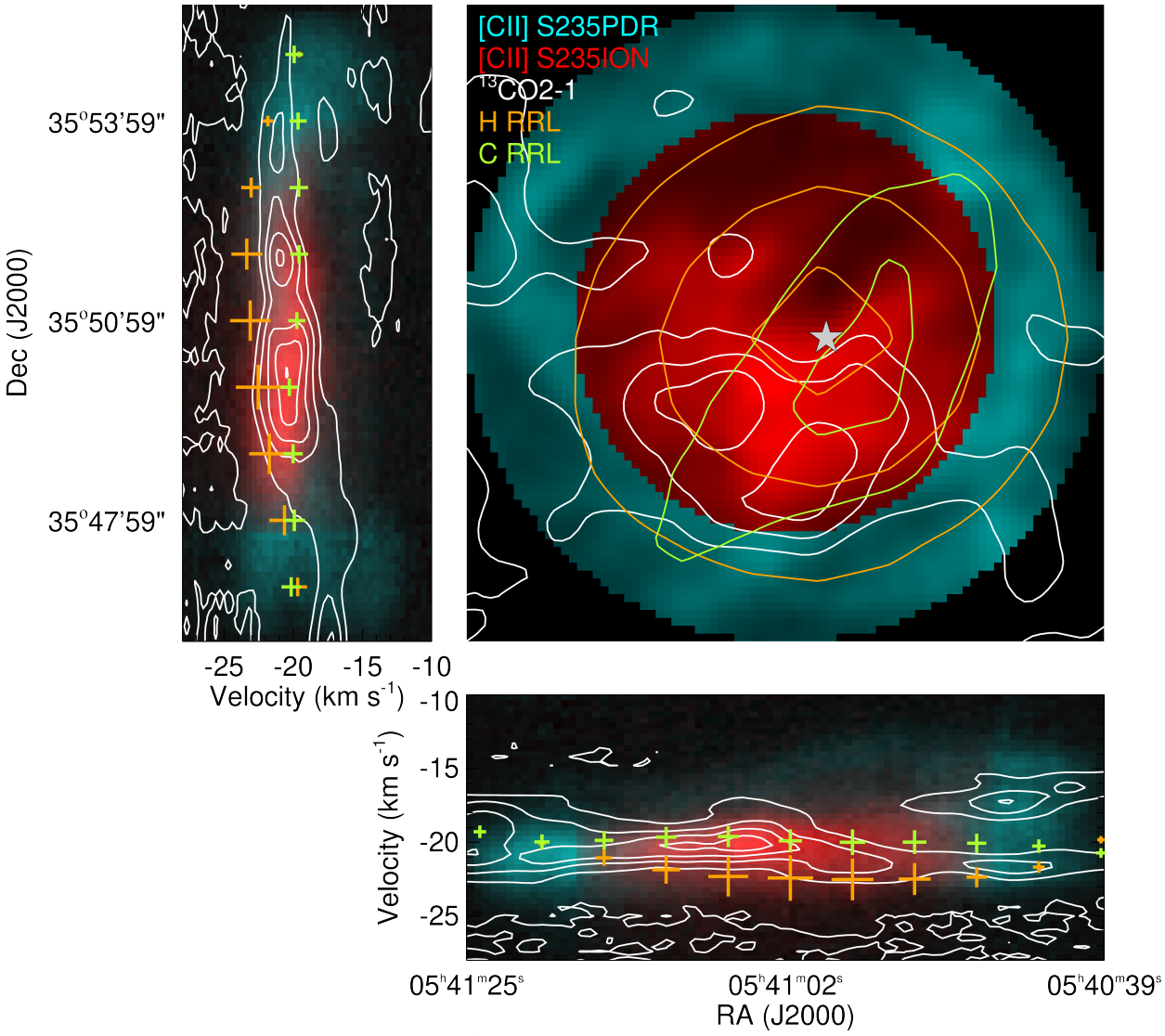

Figure 7. Position-velocity analysis of [C II] emission toward S235MAIN. The top right panel shows the moment 0 integrated intensity map from Figure 2, color coded with S235ION in red and S235PDR in cyan. White contours are of ^{13}CO 2−1 moment 0 emission (Figure 4) and green contours are of RRL moment 0 emission (Figure 3). The gray star symbol shows the location of the ionizing source. The other two panels show p-v diagrams with the same color scheme and ^{13}CO 2 − 1 contours. The green crosses show the velocity derived from Gaussian fits to RRL data integrated along a spatial direction; the size of the crosses indicate the amplitude. We plot H RRL points from the PDR even though this emission is not resolved; these points rather represent emission from the edge of the ionized hydrogen volume. [C II] emission seen in the direction of S235ION is blueshifted relative to the ionized hydrogen gas, whereas that of S235PDR is found at a broader range of velocities. We find no evidence of significant [C II] emission from the ionized hydrogen volume.

[C II] and the other tracers, as Pabst et al. (2017) found between [C II] and 8.0 μm emission in L1630. For example, Malhotra et al. (1997) show that the [C II]/IR ratio for galaxies is roughly constant at 27×10^{-3} for $L_{\rm IR} < 10^{11} L_{\odot}$. De Looze et al. (2011) claim that the $L_{\rm [C\,II]}/_{\rm FIR}$ ratio is typically linear within normal galaxies, but that it shows non-linearities for ultraluminous galaxies. Although more complicated forms of the relationship are also found in the literature (e.g., $\log(L_{\rm [C\,II]}) = A \times \log(L_{\rm IR}) + B$; Ibar et al. 2015), we prefer the simplicity of the linear relationship.

4.3.1. [C II] *and MIR data*

The strongest correlations are between [C II] and *WISE* 12 μm emission (Figure 9), for which $I_{\rm [C\,II]}$ [K km s^{-1}] $\simeq 0.89 F_{12\ \mu{\rm m}}$ [mJy] (because of the background correction, the A parameter is uncertain). The relationship is similar, and similarly strong for all investigated

Table 3. Correlations[a] between [C II] and other tracers

Tracer	Regions	A[b]	B	R^2
		K km s^{-1}	K km s^{-1}/ mJy or None	
$F_{12\,\mu m}$	S235ION	−5.01	0.89 ± 0.02	0.70
	S235PDR	−12.44	1.02 ± 0.02	0.59
	S235AB	0.64	0.71 ± 0.03	0.51
	S235C	−3.86	0.61 ± 0.02	0.85
	S235BG	−9.71	0.59 ± 0.02	0.57
	Global	−6.99	0.89 ± 0.01	0.67
$F_{22\,\mu m}$	S235ION	20.44	0.38 ± 0.01	0.44
	S235PDR	−3.61	0.89 ± 0.02	0.64
	S235AB	14.95	0.22 ± 0.01	0.54
	S235C	−13.94	0.86 ± 0.01	0.68
	S235BG	−5.73	0.79 ± 0.13	0.04
	Global	16.19	0.45 ± 0.00	0.55
$F_{1.4\,\mathrm{GHz}}$	S235ION	32.34	10.91 ± 0.30	0.36
	S235PDR	36.35	19.36 ± 0.89	0.15
	S235AB	28.55	14.86 ± 0.68	0.74
	S235C	26.69	62.88 ± 2.47	0.76
	S235BG	7.42	15.93 ± 6.66	0.04
	Global	36.74	11.14 ± 0.20	0.46
$I_{12\mathrm{CO21}}$	S235ION	19.80	0.62 ± 0.01	0.56
	S235PDR	9.39	0.33 ± 0.02	0.07
	S235AB	2.86	0.46 ± 0.21	0.18
	S235C	1.75	0.58 ± 0.16	0.00
	S235BG	3.00	0.02 ± 0.03	0.04
	Global	14.15	0.37 ± 0.02	0.23
$I_{13\mathrm{CO21}}$	S235ION	26.25	0.78 ± 0.02	0.57
	S235PDR	14.75	0.38 ± 0.02	0.12
	S235AB	−4.99	0.78 ± 0.23	0.20
	S235C	8.87	0.76 ± 0.20	0.00
	S235BG	5.18	-0.06 ± 0.11	0.01
	Global	16.08	0.47 ± 0.02	0.26
$I_{12\mathrm{CO32}}$	S235ION	30.36	1.44 ± 0.05	0.45
	S235PDR	18.66	1.06 ± 0.06	0.09
	S235AB	11.58	0.97 ± 0.39	0.04
	S235C	19.53	0.82 ± 0.38	0.00
	S235BG	3.39	0.02 ± 0.04	0.01
	Global	21.84	1.37 ± 0.05	0.23

[a] Fits made using $I_{[\mathrm{C\,II}]} = A + B \times I_\lambda$.

[b] The A-values for the *WISE* correlations are uncertain due to the absolute flux calibration of the *WISE* data.

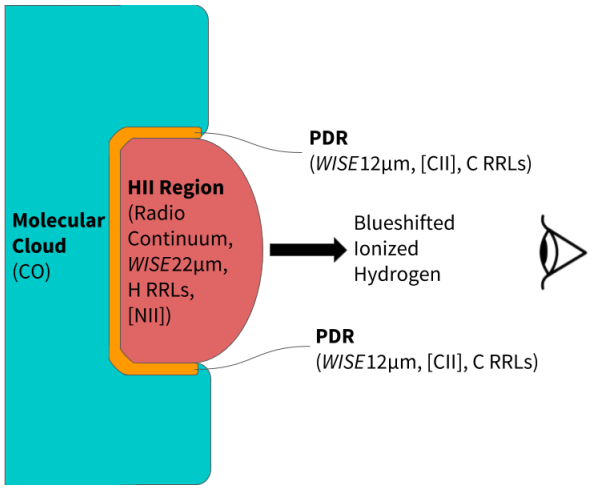

Figure 8. Cartoon model we suggest as an explanation of the velocity offset between [C II] and H RRL emission. We propose that the molecular cloud associated with S235 is behind the main region, and that the [C II] emission comes from the PDR boundary between the molecular cloud and the ionized gas.

regions of interest, including for the five background regions. We do not fit data points spatially coincident with IRS1, IRS2, the ionizing source of S235, or the star found in the north-east of the S235 PDR; data points from these locations are shown as open circles. Similarly, S235AB and S235C have contributions from point sources, and we suggest that these contributions lower the slope of the fit line. In support of this, the same trend is seen for the excluded locations coincident with IRS1 and IRS2 in S235MAIN (open circles in Figure 9).

The slope of the [C II]/12 μm relationship can be used as a proxy for the hardness of the radiation field. The 12 μm emission is caused by PAHs excited by photons with energies ~ 5 eV (Voit 1992), and carbon requires photons of energy > 11.3 eV to be ionized. Therefore, softer radiation fields will have lower [C II]/12 μm ratios. We find that the slope of the [C II]/12 μm fit in the background regions is lower than that found toward the H II regions, which is indicative of a softer UV radiation field. A softer UV field can be produced by moderate dust absorption in the diffuse medium.

The 22 μm emission is reasonably well correlated with the [C II] emission for S235AB and S235C, but is less strongly correlated for S235ION (Figure A.1). As stated previously, the 22 μm emission from H II regions is due to small dust grains heated by stellar radiation, but young stellar objects and evolved stars are also bright at 22 μm. As is the case for the 12 μm correlation, the [C II]/$F_{22\ \mu\mathrm{m}}$ correlation weakens at high values of $F_{22\ \mu\mathrm{m}}$; we again suggest that this is due to contributions to the 22 μm flux density from point sources.

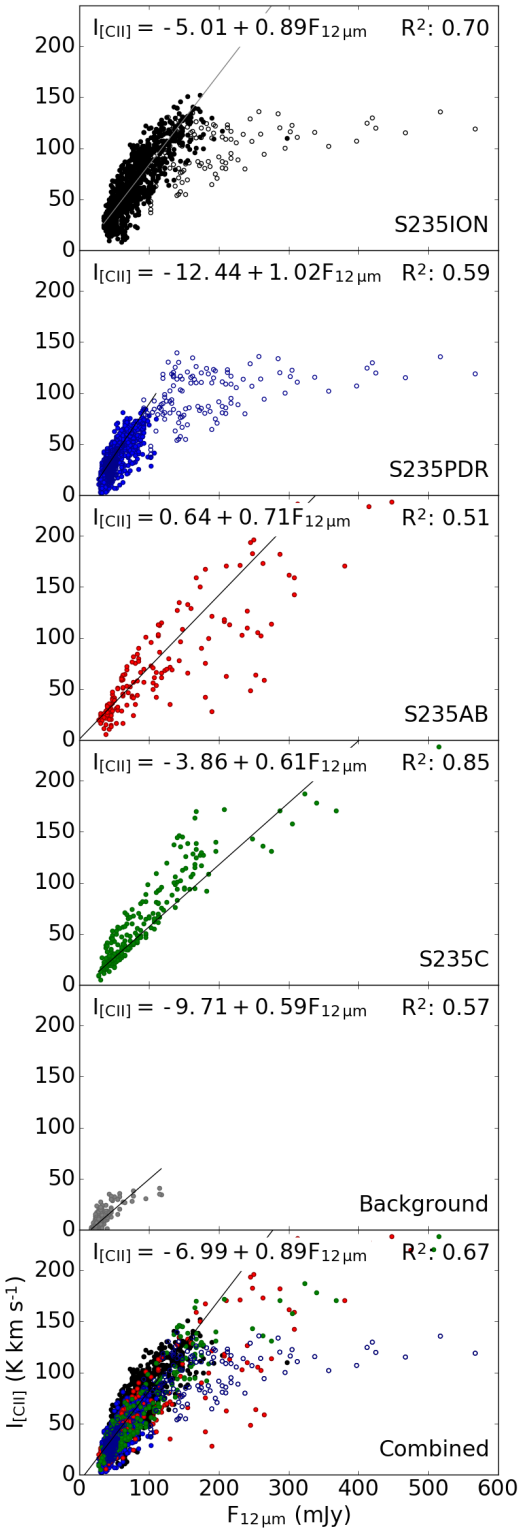

Figure 9. Correlations between [C II] and 12 μm emission in the regions of interest. The S235ION region is spatially coincident with the ionized gas of S235, S235PDR with the PDR of S235, S235AB with blended sources S235A and S235B, and S235C with H II region S235C (see Figure 2). Open circles in the top two panels are from locations of point sources; these data points are not used in the fits. The bottom panel shows data from all investigated regions. We find good correlations between [C II] and 12 μm flux density for all regions of interest.

4.3.2. [C II] *and radio continuum data*

Similar to the [C II]/22 μm correlation, the [C II]/1.4 GHz correlation is weak in the hydrogen-ionized zone and largely absent outside it (Figure 10). Importantly, the weakness of the [C II] and radio continuum correlation for S235ION indicates that the strong correlation between [C II] and 12 μm emission here is not due to the ionized hydrogen gas itself. Rather, this suggests that it is PDRs along the line of sight that are responsible for the 12 μm emission.

Despite having similar [C II] intensities and reported ionizing sources, S235AB has much higher 1.4 GHz peak flux density than S235C. The peak RRL and radio continuum emission in S235AB is much higher than that of S235C.

4.3.3. [C II] *and molecular gas*

There is a weak correlation between the strength of [C II] emission and that of molecular gas for the S235ION region (R^2 values near 0.5), but this correlation is weak for all other investigated regions (see Figures A.2). The two smaller H II regions (S235A and S235C) show weak correlations between [C II] integrated intensity and the intensity of the observed molecular gas. Evidently, the strong correlation between [C II] and molecular gas observed for entire galaxies does not hold for at the pc-scale for individual H II regions. For such small regions, even ^{13}CO may be optically thick, which would decrease the significance of the correlation. The strength of the galaxy-wide correlation is likely due to the fact that both [C II] and molecular gas trace star formation. The correlation at large scales may reflect the general relation between molecular gas and star-formation rather than local feedback physics.

4.4. *Difference maps*

We investigate spatial differences in the correlation between [C II] emission and that of the other tracers in the percentage difference maps of Figure 11. The maps give the difference between the actual [C II] intensity and the [C II] intensity that would be expected from the other tracers if they strictly followed the correlation measured for S235ION (Table 3), normalized by the measured [C II] integrated intensity. We do, however, adjust the offset (the "A" parameter in the fits) so that emission from S235ION has an average difference of zero. These maps show locations where the [C II] emission is bright relative to that expected from the other tracers (red) and where the [C II] emission is faint compared to that of the other tracers (blue). The values of the maps are therefore less important than the distribution of values.

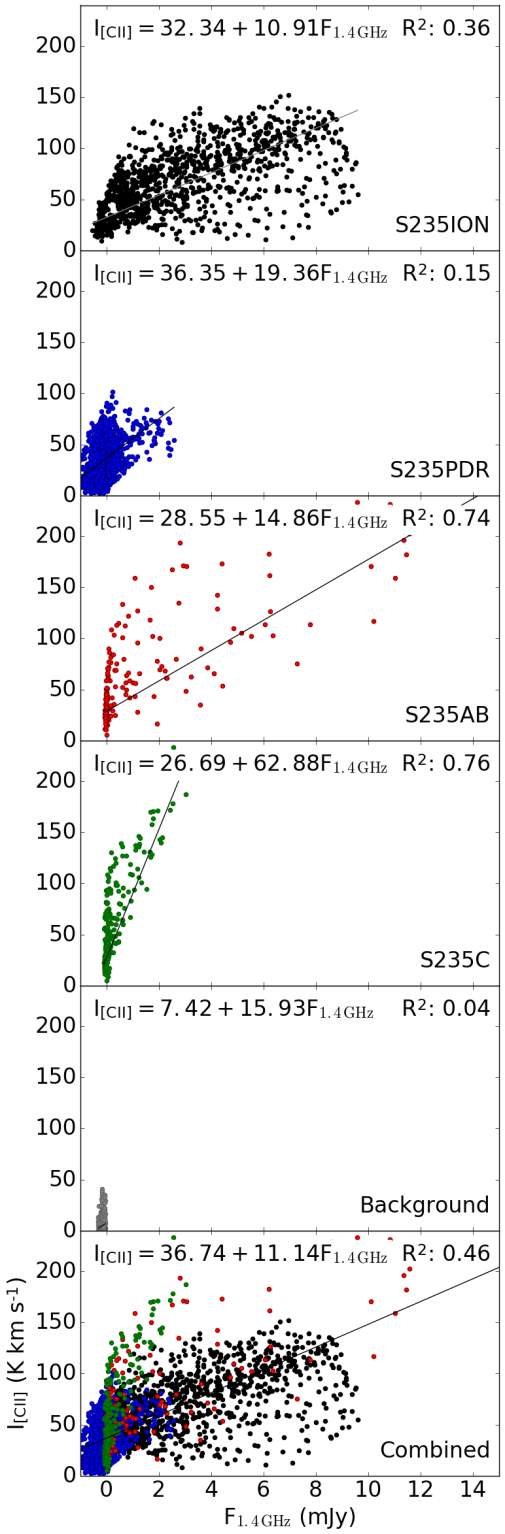

Figure 10. Correlations between 1.4 GHz intensity and that of [C II]. Panels are the same as that of Figure 9. The radio continuum emission shows a weak correlation with [C II] intensity, which indicates that they trace different ionized phases of the ISM in the S235 star-forming region.

These maps support our results from the preceding subsections. The [C II]/12 μm difference is nearly uniform across the map, indicating that there is little change in the relative intensities in the field. The [C II] versus 22 μm difference map shows that the relative intensities in the ionized hydrogen and PDR zones differ. Locations within S235ION of bright IR emission from point sources (IRS1, IRS2, and the ionizing source) appear as [C II] deficits in these panels. For the [C II]/radio continuum difference map, the ionized hydrogen zone again has different values compared with the rest of the map. Compared with [C II], there is a negligible amount of CO gas in the cavity located to the north. In the ionized hydrogen region (S235ION) and most of the PDR region (S235PDR), the CO difference maps do not show a large difference between the ionized and molecular gas components.

4.5. *Implications for extragalactic studies of* [C II]

We can use the correlations established above to investigate the implications for studies of galaxy-wide [C II] emission. The 158 μm [C II] emission line is known to be an excellent tracer of ongoing star formation, as are CO, radio continuum, and MIR emission. Therefore, we would expect a correlation between all these measures of active star formation.

We create a catalog of galaxies observed in [C II], CO, radio continuum, and *WISE* emission. We take [C II] emission line data from Brauher et al. (2008), who observed 227 galaxies in far-IR continuum and [C II] line emission using the Infrared Space Telescope. These [C II] data have an angular resolution of $\sim 85''$. We supplement the [C II] data set with [C II] observations by Stacey et al. (1991) using the Kuiper Airborne Observatory, which have an angular resolution of $\sim 55''$. We compile ^{12}CO(1 − 0) data from the FCRAO Extragalactic CO Survey (Young et al. 1995), which have an angular resolution of $46''$. For galaxies with more than one observed CO position, we choose the position closest to that of [C II]. We complement our CO and [C II] data with NVSS 1.4 GHz continuum emission data (at a resolution of $45''$) and *WISE* 12 and 22 μm data (at resolutions of $6''$ and $12''$), both compiled through spatial searches of the public point source catalogs. We attempt to remove the stellar contribution to the 12 and 22 μm fluxes by subtracting the flux at 3.5 μm, since for stars the 3.5 μm band flux is similar to that in the 12 and 22 μm bands (Nikutta et al. 2014). We determine galaxy types and angular diameters using the SIMBAD database.

The galaxies have a range of diameters from $\sim 30''$ to $\sim 1°$. Observations of each galaxy will therefore be

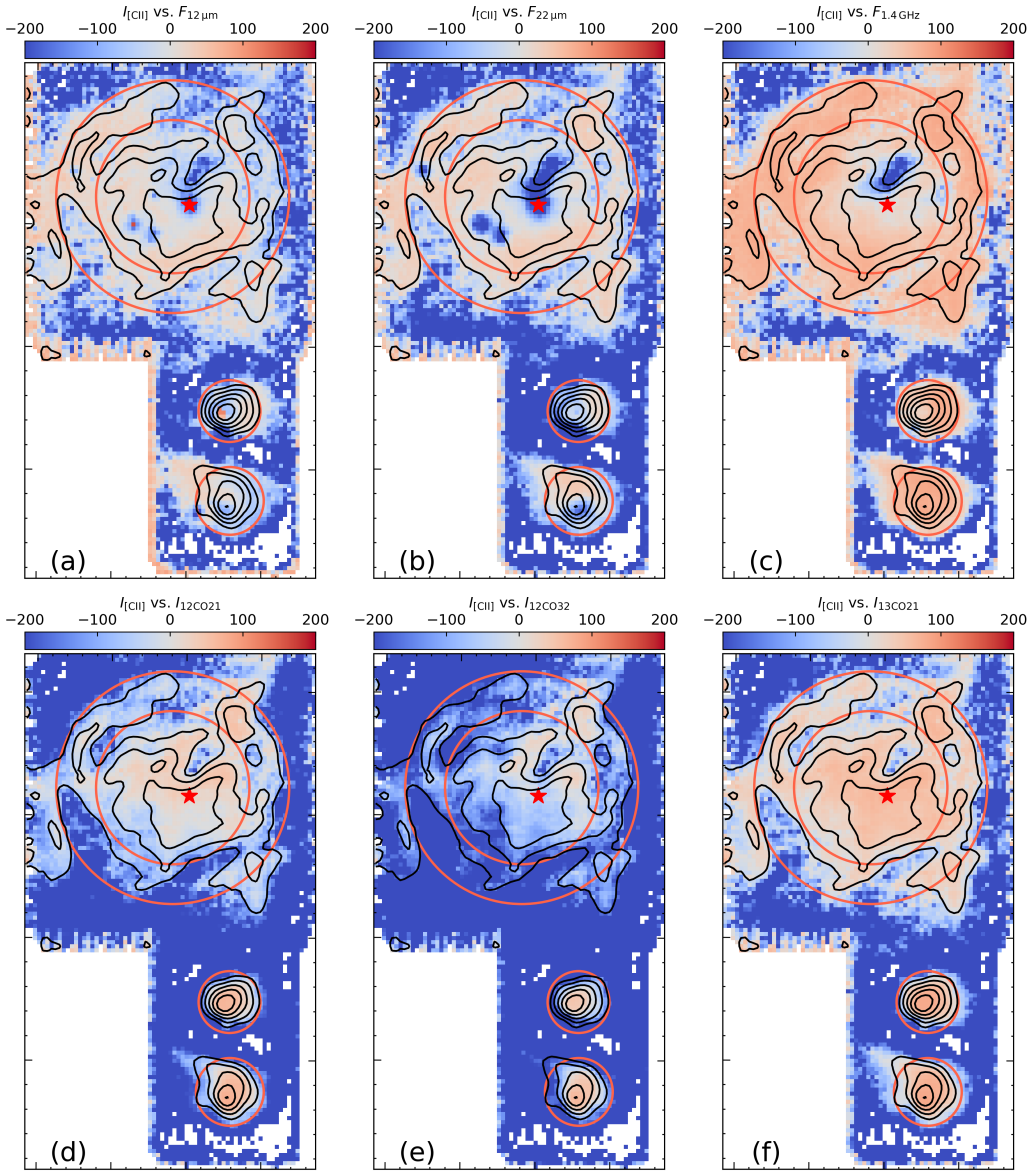

Figure 11. Intensity difference maps of [C II] and 12 μm (a), 22 μm (b), 1.4 GHz radio continuum (c), ^{12}CO($J = 2 - 1$) (d), ^{12}CO($J = 3 - 2$) (e), and ^{13}CO($J = 2 - 1$) (f). The covered area is the same as on Figure 2. The maps show locations where the [C II] emission is bright relative to the other tracers (red), and those where the [C II] emission is faint relative to the other tracers (blue). Black contours represent [C II] integrated intensity. The stars again mark the location of the ionizing source for S235.

sensitive to emission from different galactic components. For the largest galaxies, the data will contain emission only from the central region. This emission may be dominated by contributions from an older stellar population or the presence of a black hole. Observations of smaller galaxies will contain a better sampling of the total emission. To ensure that our comparisons deal with similar portions of all galaxies, we restrict our sample to those with diameters $< 150''$.

Our combined data set includes 32 galaxies: 9 active galaxies (which we call "AGN"; Simbad classifications "LIN," "Sy1,", "Sy2,", and "SyG"), 3 H II and starbursting galaxies (which we call "H II"; Simbad classifications "H2G" and "SBG"), 19 normal spiral galaxies, (which we call "Gal"; Simbad classifications "G," "GiC," "GiG," "GiP," and "IG") and 1 of other type (Simbad classification "EmG"). Nearly all galaxies in our sample have measured intensities for all tracers.

We fit a linear regression to the compiled data of the same form as before ($I_{[C\,II]} = A + BI_\lambda$) using an orthogonal distance regression (ODR), and show the results in Figure 12. An ODR minimizes the summed squared

distances between the fit and the data points, and therefore simultaneously takes into account errors on the dependent and independent variables. We perform this fit individually for AGN and normal spiral galaxies. In these figures, the asterisk on the 12 and 22 μm data represents that it is point-source corrected. We expect that the [C II] emission from H II galaxies would show good correlations with all tracers if there were sufficient data for a fit, since the [C II] emission traces ongoing star formation. The normal spirals should also have good correlations, and due to the potentially intense emission from the active nuclei themselves, the AGN correlations should be poorer.

These hypotheses are only partially born out. There are positive correlations between [C II] and the other tracers for the normal galaxies. The strongest such correlations are between [C II] and NVSS or [C II] and CO. There is no correlation between [C II] strength and that of the other tracers for the AGN sample. There are only three H II galaxies, so although we do not perform fits, the trends appear consistent with our expectations.

All the tracers provide a measurement of star formation activity. The *WISE* bands, however, may contain contributions from stars that are not removed in our method, the 1.4 GHz flux densities are potentially contaminated by the emission from central black holes (even in galaxies that are not active, like the Milky Way), and the CO integrated intensities may include contributions from CO that is not currently in the process of forming stars. That all these tracers are correlated with the integrated [C II] emission is not surprising. It is encouraging, however, that we find similarly strong correlations for the single high-mass star forming region S235 as we do for the integrated intensities from galaxies.

We are comparing results from our [C II] observations of a single H II region complex at sub-pc resolution with those integrated over entire galaxies. Results obtained at such different spatial scales should not be over-interpreted. It does, however, appear that correlations between [C II] and other SFR tracers may only exist because they all trace star formation when averaged over large areas, not because the small-scale emission properties are related.

5. SUMMARY

We compared *SOFIA* observations of [C II] 158 μm emission with *WISE* MIR 12 μm and 22 μm data, NVSS 1.4 GHz radio continuum data, and molecular data (^{12}CO (2 − 1), ^{12}CO (3 − 2), ^{13}CO (2 − 1)) toward the star formation complex Sh2-235. The main purpose of the present study is to determine where [C II] emission arises, relative to the emission from tracers of different phases of the ISM. We analyzed emission from four regions of interest representing the inner ionized hydrogen in the main H II region S235, the PDR of S235, and the two smaller H II regions in the field, S235A and S235C. We also sampled the diffuse background emission in five locations.

Roughly half of the [C II] emission in S235 originates in the direction of the ionized hydrogen region, mainly close to the location of the central ionizing star. The remaining [C II] emission in the S235 region arises from the filamentary PDR surrounding the ionized region. This direction toward the ionized hydrogen also includes potential contributions from front- and back-side PDRs along the line of sight. We find little evidence that the [C II] emission seen in the direction of the ionized hydrogen is actually from the ionized hydrogen volume; the data instead are consistent with [C II] emission seen in the direction of the ionized hydrogen originating in the back-side PDR. Our results therefore are similar to those of Pabst et al. (2017) and Goicoechea et al. (2015) that no more than 10% of the [C II] emission is cospatial with the ionized hydrogen gas. The two additional small H II regions in the field have similar [C II] emission strengths, despite very different radio continuum strengths.

The [C II] emission is strongly correlated with *WISE* 12 μm intensity across the entire field. The correlation holds for all three H II regions, and is also reasonably strong for the background regions. This indicates that 12 μm intensity can predict [C II] intensity from H II regions at various evolutionary stages ionized by O and early B-type stars having a range of ionizing fluxes, and also from diffuse C^+ gas. The UV radiation field found in H II region PDRs excites emission in the *WISE* 12 μm band and also ionizes carbon, leading to [C II] emission. The 12 μm band traces emission from PAHs and warm dust. PAHs fluoresce when hit by soft-UV photons ($E \gtrsim 5$ eV; Voit 1992), and ionized carbon is created by photons with $E > 11.3$ eV. Both [C II] and 12 μm emission trace emission from surfaces irradiated by ultraviolet photons. They are therefore surface rather than volume tracers. We expect the same relationship between [C II] and *Spitzer* 8.0 μm data (Pabst et al. 2017), since the *WISE* 12 μm and *Spitzer* 8.0 μm band emission are themselves strongly correlated for H II regions (Anderson et al. 2014; Makai et al. 2017).

Radio continuum and *WISE* 22 μm emission are both centrally peaked surrounding the ionizing source of S235. The correlation between [C II] emission and *WISE* 22 μm emission is weaker that that found for *WISE* 12 μm data. The correlation between [C II] emission and 1.4 GHz radio continuum is only apparent toward the ionized hydrogen gas, and is weak toward the PDR.

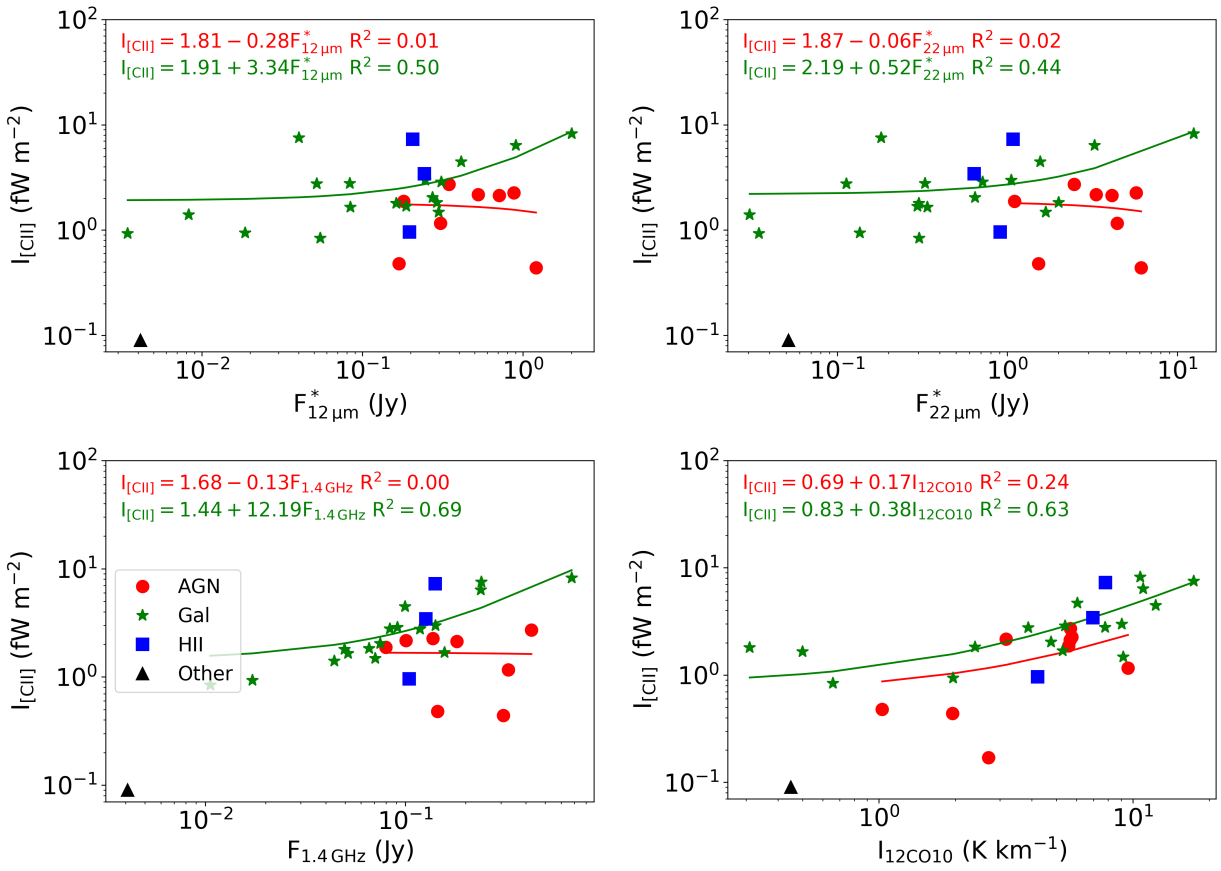

Figure 12. Correlations between [C II] and *WISE* 12 μm emission (top left) *WISE* 22 μm emission (top right) NVSS 1.4 GHz emission (bottom left), and ^{12}CO (1 – 0) emission (bottom right) for various galaxy types. For normal and starbursting galaxies, the correlations are similar to what was found for S235.

This further supports the idea that the [C II]/12 μm correlation found toward the ionized gas of S235 is in large part caused by line-of-sight PDRs. The 1.4 GHz radio continuum traces emission from ionized hydrogen. The lack of good spatial correlation with the [C II] emission indicates that we observe emission from different ionized gas components in S235.

Averaged over entire spiral galaxies, we see similar trends; the intensity of [C II] and *WISE* data are correlated, although weakly so. We find modest correlations between [C II] and NVSS 1.4 GHz intensities, as well as between [C II] and ^{12}CO(1 – 0) intensities, for normal spiral galaxies. Galaxies hosting AGN show poor correlations.

Therefore, although many tracers are correlated with the strength of [C II] emission, only *WISE* 12 μm emission is correlated on small scales within S235, as well as averaged over entire galaxies. Further [C II] observations of a larger sample of Galactic H II regions would allow us to determine if our results for S235 are representative.

This work is based on observations made with the NASA/DLR Stratospheric Observatory for Infrared Astronomy (*SOFIA*). *SOFIA* is jointly operated by the Universities Space Research Association, Inc. (USRA), under NASA contract NAS2-97001, and the Deutsches SOFIA Institut (DSI) under DLR contract 50 OK 0901 to the University of Stuttgart. We thank West Virginia University for its financial support of GBT operations, which enabled some of the observations for this project. This research has made use of NASAs Astrophysics Data System Bibliographic Services and the SIMBAD database operated at CDS, Strasbourg, France. This publication makes use of data products from *WISE*, which is a joint project of the University of California, Los Angeles, and the Jet Propulsion Laboratory/California Institute of Technology, funded by the National Aeronautics and Space Administration.

Financial support for this work was provided by NASA through awards #04 – 0132 and #05 – 0061 issued by USRA to LDA. VO was supported by Deutsche Forschungsgemeinschaft (DFG) within the Collaborative Research Center 956, project C1 - project ID

184018867. NS acknowledges support by the french ANR and the German DFG through the project "GENESIS" (ANR-16-CE92-0035-01/DFG1591/2-1) and funding by the Bundesministerium für Wirtschaft und Energie through the grant MOBS (50OR1714). MSK was supported by Russian Foundation for Basic Research, grant number 18-32-20049. AMS was supported by Russian Foundation for Basic Research, grant 18-02-00917 and by the Act 211 Government of the Russian Federation, agreement No. 02.A03.21.0006.

Facility: *SOFIA*, GBT

Software: AstroPy (Astropy Collaboration et al. 2013; Price-Whelan et al. 2018), AplPy (Robitaille & Bressert 2012; Robitaille 2019), IDL

REFERENCES

Abel, N. P. 2006, MNRAS, 368, 1949

Akimkin, V. V., Kirsanova, M. S., Pavlyuchenkov, Y. N., & Wiebe, D. S. 2015, MNRAS, 449, 440

—. 2017, MNRAS, 469, 630

Allen, L. E., Hora, J. L., Megeath, S. T., et al. 2005, in IAU Symposium, Vol. 227, Massive Star Birth: A Crossroads of Astrophysics, ed. R. Cesaroni, M. Felli, E. Churchwell, & M. Walmsley, 352–357

Alves, M. I. R., Calabretta, M., Davies, R. D., et al. 2015, MNRAS, 450, 2025

Anderson, L. D., Armentrout, W. P., Johnstone, B. M., et al. 2015, ApJS, 221, 26

Anderson, L. D., Armentrout, W. P., Luisi, M., et al. 2018, ApJS, 234, 33

Anderson, L. D., Bania, T. M., Balser, D. S., et al. 2014, ApJS, 212, 1

Anderson, L. D., Bania, T. M., Balser, D. S., & Rood, R. T. 2011, ApJS, 194, 32

Astropy Collaboration, Robitaille, T. P., Tollerud, E. J., et al. 2013, A&A, 558, A33

Balser, D. S. 2006, AJ, 132, 2326

Bieging, J. H., Patel, S., Peters, W. L., et al. 2016, ApJS, 226, 13

Boley, P. A., Sobolev, A. M., Krushinsky, V. V., et al. 2009, MNRAS, 399, 778

Boselli, A., Gavazzi, G., Lequeux, J., & Pierini, D. 2002, A&A, 385, 454

Brauher, J. R., Dale, D. A., & Helou, G. 2008, ApJS, 178, 280

Brown, A. G. A. 2018, in IAU Symposium, Vol. 330, IAU Symposium, ed. A. Recio-Blanco, P. de Laverny, A. G. A. Brown, & T. Prusti, 13–22

Burns, R. A., Imai, H., Handa, T., et al. 2015, MNRAS, 453, 3163

Camargo, D., Bonatto, C., & Bica, E. 2011, MNRAS, 416, 1522

Chavarría, L., Allen, L., Brunt, C., et al. 2014, MNRAS, 439, 3719

Condon, J. J., Cotton, W. D., Greisen, E. W., et al. 1998, AJ, 115, 1693

Crawford, M. K., Genzel, R., Townes, C. H., & Watson, D. M. 1985, ApJ, 291, 755

Croxall, K. V., Smith, J. D., Pellegrini, E., et al. 2017, ApJ, 845, 96

De Looze, I., Baes, M., Fritz, J., Bendo, G. J., & Cortese, L. 2011, Baltic Astronomy, 20, 463

Dewangan, L. K., & Anandarao, B. G. 2011, MNRAS, 414, 1526

Dewangan, L. K., & Ojha, D. K. 2017, ApJ, 849, 65

Dewangan, L. K., Ojha, D. K., Luna, A., et al. 2016, ApJ, 819, 66

Draine, B. T. 2011, ApJ, 732, 100

Evans, II, N. J., & Blair, G. N. 1981, ApJ, 246, 394

Felli, M., Testi, L., Valdettaro, R., & Wang, J.-J. 1997, A&A, 320, 594

Georgelin, Y. M., Georgelin, Y. P., & Roux, S. 1973, A&A, 25, 337

Goicoechea, J. R., Santa-Maria, M. G., Bron, E., et al. 2018, arXiv e-prints, arXiv:1812.00821

Goicoechea, J. R., Teyssier, D., Etxaluze, M., et al. 2015, ApJ, 812, 75

Graf, U. U., Simon, R., Stutzki, J., et al. 2012, A&A, 542, L16

Heyminck, S., Graf, U. U., Güsten, R., et al. 2012, A&A, 542, L1

Hollenbach, D. J., & Tielens, A. G. G. M. 1999, Reviews of Modern Physics, 71, 173

Ibar, E., Lara-López, M. A., Herrera-Camus, R., et al. 2015, MNRAS, 449, 2498

Israel, F. P., & Felli, M. 1978, A&A, 63, 325

Jones, A. P. 2004, in Astronomical Society of the Pacific Conference Series, Vol. 309, Astrophysics of Dust, ed. A. N. Witt, G. C. Clayton, & B. T. Draine, 347

Kirsanova, M. S., Sobolev, A. M., Thomasson, M., et al. 2008, MNRAS, 388, 729

Kirsanova, M. S., Wiebe, D. S., Sobolev, A. M., Henkel, C., & Tsivilev, A. P. 2014, MNRAS, 437, 1593

Kloosterman, J., Cottam, T., Swift, B., et al. 2012, in Proc. SPIE, Vol. 8452, Millimeter, Submillimeter, and Far-Infrared Detectors and Instrumentation for Astronomy VI, 845204

Krishna Swamy, K. S., & O'dell, C. R. 1967, ApJ, 147, 529

Lafon, G., Deharveng, L., Baudry, A., & de La Noë, J. 1983, A&A, 124, 1

Langer, W. D., Velusamy, T., Pineda, J., et al. 2011, in EAS Publications Series, Vol. 52, EAS Publications Series, ed. M. Röllig, R. Simon, V. Ossenkopf, & J. Stutzki, 161–164

Liu, B., McIntyre, T., Terzian, Y., et al. 2013, AJ, 146, 80

Luisi, M., Anderson, L. D., Bania, T. M., et al. 2018, PASP, 130, 084101

Madden, S. C., Geis, N., Genzel, R., et al. 1993, ApJ, 407, 579

Makai, Z., Anderson, L. D., Mascoop, J. L., & Johnstone, B. 2017, ApJ, 846, 64

Malhotra, S., Helou, G., Stacey, G., et al. 1997, ApJL, 491, L27

Minkowski, R. 1946, PASP, 58, 305

Nikutta, R., Hunt-Walker, N., Nenkova, M., Ivezić, Ž., & Elitzur, M. 2014, MNRAS, 442, 3361

Nordh, H. L., Fridlund, C. V. M., van Duinen, R. J., et al. 1984, A&A, 131, 221

Ossenkopf, V., Rollig, M., Cubick, M., & Stutzki, J. 2007, in Molecules in Space and Laboratory, 95

Pabst, C., Higgins, R., Goicoechea, J. R., et al. 2019, Nature, 565, 618

Pabst, C. H. M., Goicoechea, J. R., Teyssier, D., et al. 2017, A&A, 606, A29

Pety, J. 2005, in SF2A-2005: Semaine de l'Astrophysique Francaise, ed. F. Casoli, T. Contini, J. M. Hameury, & L. Pagani, 721

Pilbratt, G. L., Riedinger, J. R., Passvogel, T., et al. 2010, A&A, 518, L1

Pineda, J. L., Langer, W. D., Velusamy, T., & Goldsmith, P. F. 2013, A&A, 554, A103

Price-Whelan, A. M., Sipőcz, B. M., Günther, H. M., et al. 2018, AJ, 156, 123

Quireza, C., Rood, R. T., Balser, D. S., & Bania, T. M. 2006, ApJS, 165, 338

Relaño, M., Kennicutt, R., Lisenfeld, U., et al. 2016, A&A, 595, A43

Rho, J., Reach, W. T., Lefloch, B., & Fazio, G. G. 2006, ApJ, 643, 965

Rigopoulou, D., Hurley, P. D., Swinyard, B. M., et al. 2013, MNRAS, 434, 2051

Risacher, C., Güsten, R., Stutzki, J., et al. 2016, A&A, 595, A34

Robitaille, T. 2019, APLpy v2.0: The Astronomical Plotting Library in Python, , , doi:10.5281/zenodo.2567476

Robitaille, T., & Bressert, E. 2012, APLpy: Astronomical Plotting Library in Python, Astrophysics Source Code Library, , , ascl:1208.017

Robitaille, T. P., Churchwell, E., Benjamin, R. A., et al. 2012, A&A, 545, A39

Roser, J. E., & Ricca, A. 2015, ApJ, 801, 108

Sarazin, C. L. 1977, ApJ, 211, 772

Schneider, N., Stutzki, J., Winnewisser, G., Poglitsch, A., & Madden, S. 1998, A&A, 338, 262

Schneider, N., Röllig, M., Simon, R., et al. 2018, A&A, 617, A45

Sharpless, S. 1959, ApJS, 4, 257

Silverglate, P. R., & Terzian, Y. 1978, ApJ, 224, 437

Simon, R., Schneider, N., Stutzki, J., et al. 2012, A&A, 542, L12

Stacey, G. J., Geis, N., Genzel, R., et al. 1991, ApJ, 373, 423

Tielens, A. G. G. M. 2008, ARA&A, 46, 289

Vallee, J. P. 1987, AJ, 93, 204

Voit, G. M. 1992, MNRAS, 258, 841

Winkel, B., Kerp, J., Flöer, L., et al. 2016, A&A, 585, A41

Wolfire, M. G., Hollenbach, D., & Tielens, A. G. G. M. 1989, ApJ, 344, 770

Wright, E. L., Eisenhardt, P. R. M., Mainzer, A. K., et al. 2010, AJ, 140, 1868

Young, E. T., Becklin, E. E., Marcum, P. M., et al. 2012, ApJL, 749, L17

Young, J. S., Xie, S., Tacconi, L., et al. 1995, ApJS, 98, 219

APPENDIX

A. CORRELATIONS BETWEEN [C II] 22μm EMISSION AND BETWEEN [C II] AND MOLECULAR GAS EMISSION

Here, we show correlations between the intensity of integrated [C II] emission and the intensities of *WISE* 22 μm and CO emission. The parameters of the fits shown in the figures are given in Table 3. For all figures in this appendix, the symbols, panels and fits are similar to those in Figures 9 and 10.

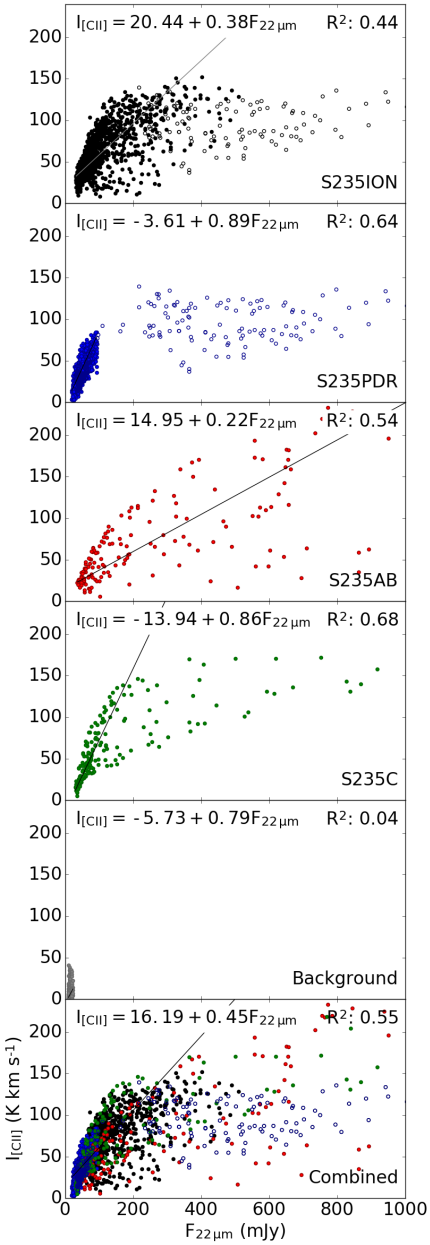

Figure A.1. Correlations between 22 μm intensity and that of [C II]. The S235ION region is spatially coincident with the ionized gas of S235, S235PDR with the PDR of S235, S235AB with blended sources S235A and S235B, and S235C with H II region S235C (see Figure 2). The 22 μm emission shows a good correlation with the [C II] emission, albeit with larger spread than the 12 μm emission (Figure 9). As seen in Figure 4, much of the 22 μm emission arises near to the central ionizing star.

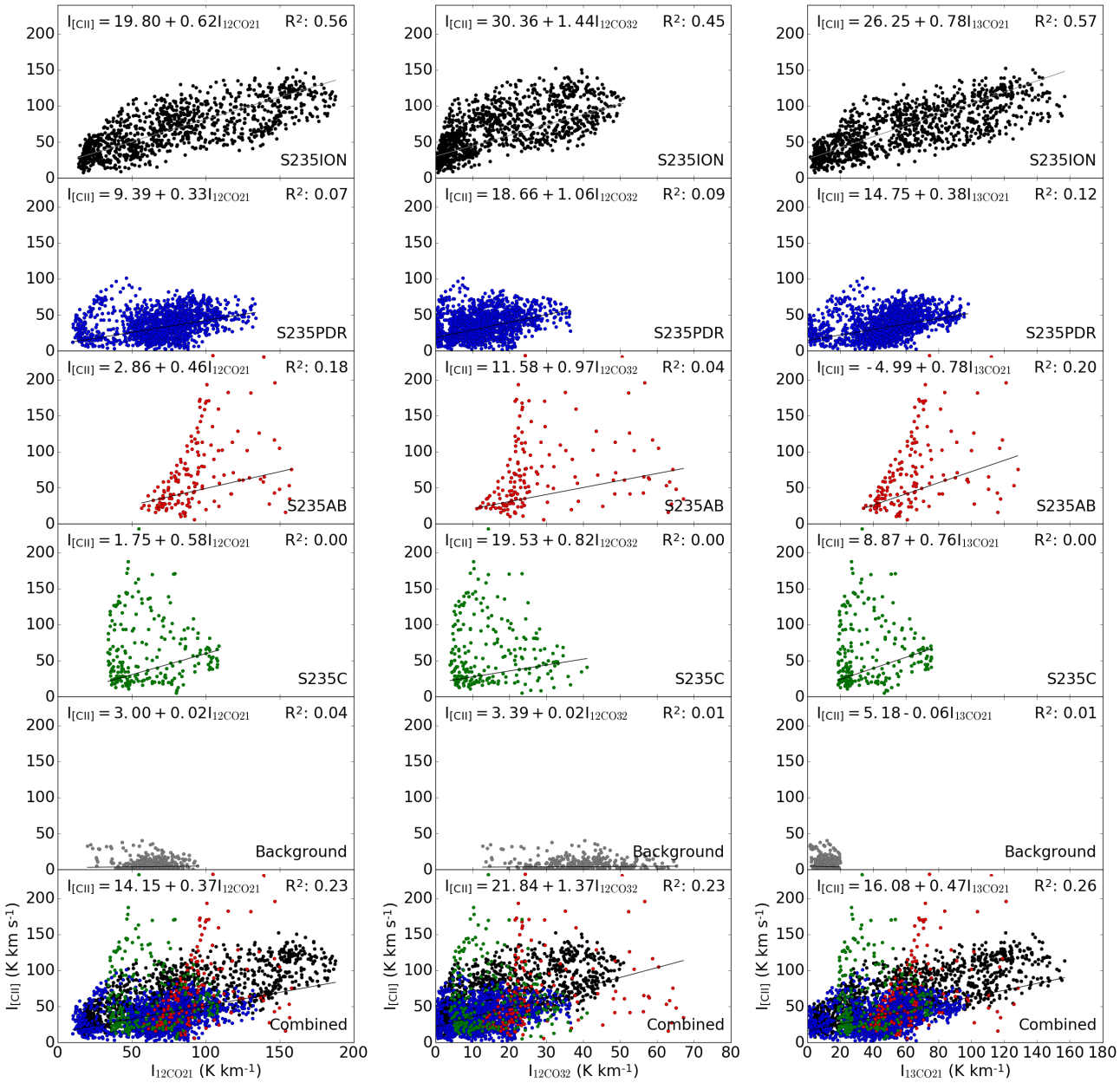

Figure A.2. Correlation between CO intensity and that of [C II], for ^{12}CO $2-1$ (left), ^{12}CO $3-2$ (middle), and ^{13}CO $2-1$ (right). The S235ION region is spatially coincident with the ionized gas of S235, S235PDR with the PDR of S235, S235AB with blended sources S235A and S235B, and S235C with H II region S235C (see Figure 2). The large spread of the data points may indicate that a significant amount of the ionized carbon is not associated with CO gas in the S235 star formation complex.